J. Fluid Mech. (2018), *vol.* 835, *pp.* 102–130.
doi:10.1017/jfm.2017.728

Premixed turbulent flame speed in an oscillating disturbance field

Luke J. Humphrey[1], **Benjamin Emerson**[1] **and Tim C. Lieuwen**[1,†]

[1]School of Aerospace Engineering, Georgia Institute of Technology, Atlanta, GA 30313, USA

(Received 19 January 2017; revised 15 July 2017; accepted 5 October 2017;
first published online 27 November 2017)

This paper considers the manner in which turbulent premixed flames respond to a superposition of turbulent and narrowband disturbances. This is an important fundamental problem that arises in most combustion applications, as turbulent flames exist in hydrodynamically unstable flow fields and/or in confined systems with narrowband acoustic waves. This paper presents the first measurements of the sensitivity of the turbulent displacement speed to harmonically oscillating flame wrinkles. The flame is attached to a transversely oscillating, heated wire, resulting in the introduction of coherent, convecting wrinkles on the flame. The approach flow turbulence is varied systematically using a variable turbulence generator, enabling quantification of the effect of turbulent flow disturbances on the harmonic wrinkles. Mie scattering measurements are used to quantify the flame edge dynamics, while high speed particle image velocimetry is used to measure the flow field characteristics. By ensemble averaging the results, the ensemble-averaged flame edge and flow characteristics are recovered. For low turbulence intensities, sharp cusps are present in the negative curvature regions of the ensemble-averaged flame position, similar to laminar flames. These cusps are smoothed out at high turbulence intensities. The coherent, ensemble-averaged flame wrinkle amplitude decays with increasing turbulence intensity and with downstream distance. In addition, the ensemble-averaged turbulent flame speed is modulated in space and time. The most significant result of these measurements is the clear demonstration of the correlation between the ensemble-averaged turbulent flame speed and ensemble-averaged flame curvature, with the phase-dependent flame speed increasing in regions of negative curvature. These results have important implications on turbulent combustion physics and modelling, since quasi-coherent velocity disturbances are nearly ubiquitous in shear driven, high turbulent flows and/or confined systems with acoustic feedback. Specifically, these data clearly show that nonlinear interactions occur between the multi-scale turbulent disturbances and the more narrowband disturbances associated with coherent structures. In other words, conceptual models of the controlling physics in combustors with shear driven turbulence must account for the fundamentally different effects of spectrally distributed turbulent disturbances and more narrowband, quasi-coherent disturbances.

Key words: combustion, turbulent reacting flows

† Email address for correspondence: tim.lieuwen@aerospace.gatech.edu

1. Introduction

Turbulent combustion is a subset of a broader class of problems investigating how flames respond to disturbances – such disturbances could be stochastic, impulsive, time harmonic as well as a superposition of these disturbances. This paper considers the turbulent combustion problem for premixed flames responding to a superposition of turbulent and narrowband disturbances.

This problem naturally arises in several applications, such as the general problem of turbulent flames in hydrodynamically unstable flow fields, where significant narrowband energy exists in large-scale organized vortices. This problem also naturally arises in confined systems which experience thermoacoustic instabilities, which can result from the self-excited feedback between heat release and narrowband acoustic oscillations (Balachandran *et al.* 2005; Kabiraj & Sujith 2012; Magri & Juniper 2013). These oscillations are particularly problematic in premixed combustors and can lead to blowoff, flashback, degraded system performance and increased maintenance requirements (Lieuwen & Yang 2005). One of the least understood parts of the feedback loop between acoustic and velocity oscillations and heat release is how turbulent flames respond to narrowband oscillations.

A considerable research effort has focused on the response of laminar flames to harmonic flow disturbances, and the key physics controlling both the local space–time dynamics of the flame position (Petersen & Emmons 1961; Boyer & Quinard 1990; Fleifil *et al.* 1996; Truffaut & Searby 1999; Searby, Truffaut & Joulin 2001; Preetham, Santosh & Lieuwen 2008; Matalon 2009; Shanbhogue *et al.* 2009; Shin & Lieuwen 2012) and spatially integrated heat release (Ducruix, Durox & Candel 2000; Santosh & Sujith 2005; Kashinath, Hemchandra & Juniper 2013; Humphrey *et al.* 2014) are well understood.

However, real flames inevitably exist in a turbulent flow environment, and so the flame is simultaneously disturbed by both spatio-temporally narrowband acoustic and/or hydrodynamic disturbances and broadband turbulence fluctuations. A large body of research has attempted to understand and predict averaged turbulent burning speeds (Driscoll 2008). These burning velocities can be defined based upon consumption- or displacement-based flame speed definitions (Poinsot & Veynante 2005). Displacement speeds are defined as the velocity of the flow normal to some reference isosurface. In contrast, consumption speeds are defined from volume integrated consumption rates, suitably normalized by a reference area. It is also important to differentiate between instantaneous flame speeds and those based upon time or ensemble averages, as turbulent flame speeds are. It is well known that laminar displacement and consumption speeds are functions of flame stretch and curvature, with a sensitivity that is controlled by the Lewis number and relative mass diffusion rates of fuel and oxidizer (Candel & Poinsot 1990; Law & Sung 2000; Matalon 2009). These laminar displacement and consumption speeds can exhibit quite different trends in highly unsteady flows or in flows with very high stretch levels. For example, computational studies for lean methane flames compute instantaneous flame speeds, and discuss merging and annihilation of opposing flame surfaces in regions of strong negative curvature (Gran, Echekki & Chen 1996; Chen & Im 1998). A common finding is the observation of negative instantaneous displacement speeds, while consumption speeds are always positive.

In turbulent flows, a variety of studies have looked at instantaneous displacement speeds and their correlations with instantaneous curvature and flame stretch (Gran *et al.* 1996; Chen & Im 1998; Kerl, Lawn & Beyrau 2013; Trunk *et al.* 2013). For example, a number of direct numerical simulation studies (Baum *et al.* 1994;

Hawkes & Chen 2004, 2006; Sankaran *et al.* 2007) of turbulent, premixed flames in the thin reaction zone regime confirm correlations between local flame speed and flame strain/curvature that are consistent with laminar flame theory, although there is significant scatter in these results. This scatter is due to unsteady effects (which cause the flame speed to lag the instantaneous strain rate), as well as the different sensitivity of the flame speed to strain and curvature for unsteady and highly stretched flames. These results provide useful analogies for those discussed in § 3, but it is important to recall that the underlying physics driving the displacement speed trends for instantaneous flamelets versus time/ensemble averaged progress variable contours can be quite different.

As presented above, past research has addressed both averaged global turbulent flame speeds as well as local flamelet speeds and their dependence on local curvature. However, investigations of the interaction between broadband turbulence and narrowband harmonic disturbances are still relatively sparse, as reviewed below. Moreover, because the flame dynamics is nonlinear, the influence of these disturbances on the flame cannot be treated additively (Hemchandra, Preetham & Lieuwen 2007; Hemchandra, Peters & Lieuwen 2011; Shin & Lieuwen 2013).

Hemchandra *et al.* (2007) computationally investigated a turbulent, premixed flame perturbed by harmonic, travelling disturbances and presented ensemble-averaged results from these calculations, thus enabling analysis of the coherent flame wrinkles which are otherwise obscured by the effects of turbulent disturbances on the flame. They found that kinematic restoration (i.e. the smoothing effect of flame propagation normal to itself) diminishes the amplitude of the wrinkles induced by harmonic forcing, and that this effect is enhanced with increasing turbulence. Following this work, Shin & Lieuwen (2013) performed a numerical investigation of ensemble-averaged flame sheet dynamics for a turbulent, premixed isothermal flame anchored on a harmonically oscillating bluff body. They were able to further characterize several key effects of turbulence on the ensemble-averaged flame response. First, the introduction of turbulence, as with the study by Hemchandra *et al.* (2007), smoothed the cusps which result from harmonic forcing and reduced the amplitude of coherent flames wrinkles relative to laminar flames. In the near field, this smoothing is due to phase jitter and kinematic restoration associated with fine-scale turbulent wrinkles. In the far field, the increase in turbulent flame speed accelerates the smoothing of the large-scale harmonically induced flame wrinkles.

In addition, Shin & Lieuwen (2013) introduced an explicit governing equation for the ensemble-averaged flame position. This definition for the ensemble-averaged flame is analogous to the method commonly used for flamelets, based on the front-tracking (G-equation) approach, which is commonly used in other studies of flame kinematics and turbulent flame speed (Matalon & Matkowsky 1982; Williams 1985; Kerstein, Ashurst & Williams 1988; Boyer & Quinard 1990; Fleifil *et al.* 1996; Dowling 1999; Peters, Wenzel & Williams 2000; Lipatnikov & Sathiah 2005; Santosh & Sujith 2005; Shanbhogue *et al.* 2009; Matalon & Creta 2012; Shin & Lieuwen 2012). In the limit where the flame is thin relative to the scales of the flow and can be treated as a flow discontinuity, the flame is defined as the zero surface given by the G-equation:

$$\frac{\partial G}{\partial t} + \boldsymbol{u} \cdot \nabla G = S_L |\nabla G|, \tag{1.1}$$

where G is a scalar variable, $\boldsymbol{u}$ is the flow velocity at the flame front and S_L denotes the local propagation front speed. For a single valued flame position, this equation can

be written as:

$$\frac{\partial \xi}{\partial t} + u_s \frac{\partial \xi}{\partial s} - u_n + u_z \frac{\partial \xi}{\partial z} = S_L \left[1 + \left(\frac{\partial \xi}{\partial z} \right)^2 + \left(\frac{\partial \xi}{\partial s} \right)^2 \right]^{1/2}, \tag{1.2}$$

where ξ denotes the position of the instantaneous flame, and s is the downstream coordinate for a coordinate system aligned with the unforced flame position, as shown in figure 6. The velocity components in the flame tangential, normal, and transverse directions are u_s, u_n and u_z respectively. Before discussing the application of this approach to ensemble-averaged, turbulent flames, we introduce some necessary nomenclature. First, the flame and flow variables can be expanded as: $\boldsymbol{u}(\boldsymbol{s}, t) = \boldsymbol{u}_0(\boldsymbol{s}) + \boldsymbol{u}_1(\boldsymbol{s}, t) + \boldsymbol{u}_2(\boldsymbol{s}, t)$, where $()_0$ is the time-averaged quantity, defined as $\boldsymbol{u}_0(\boldsymbol{s}) = 1/T \int_0^T \boldsymbol{u}(\boldsymbol{s}, t)\, \mathrm{d}t$. The quantity, $()_1$, is the coherent fluctuation and is defined using the ensemble average, denoted by the operator $\langle\,\rangle$, as $\boldsymbol{u}_1(\boldsymbol{s}, t) = \langle \boldsymbol{u}(\boldsymbol{s}, t) - \boldsymbol{u}_0(\boldsymbol{s}) \rangle$. The random fluctuation, $()_2$, is $\boldsymbol{u}_2(\boldsymbol{s}, t) = \boldsymbol{u}(\boldsymbol{s}, t) - \boldsymbol{u}_0(\boldsymbol{s}) - \boldsymbol{u}_1(\boldsymbol{s}, t)$. Second, note that $(\boldsymbol{u}_1)_0 = (\boldsymbol{u}_2)_0 = 0$, $\langle \boldsymbol{u}_2 \rangle = 0$, but $\langle \boldsymbol{u}_1 \rangle \neq 0$. For this harmonically forced problem, the 'ensemble average' is equivalent to a 'phase average'. However, note that the phase average should not be confused with an average taken over the all points of phase in a forcing cycle.

In analogy with (1.2), above, Shin & Lieuwen (2013) wrote the following equation relating the ensemble-averaged flame position to the ensemble-averaged disturbance field:

$$\begin{aligned} &\frac{\partial \langle \xi \rangle}{\partial \hat{t}} + \langle \underset{\sim}{u}_s(s, \hat{t}) \rangle \frac{\partial \langle \xi(s, \hat{t}) \rangle}{\partial s} - \langle \underset{\sim}{u}_n(s, \hat{t}) \rangle + \langle \underset{\sim}{u}_z(s, \hat{t}) \rangle \frac{\partial \langle \xi(s, \hat{t}) \rangle}{\partial z} \\ &\quad = S_{T,D}(s, z, \hat{t}) \left[1 + \left(\frac{\partial \langle \xi(s, \hat{t}) \rangle}{\partial z} \right)^2 + \left(\frac{\partial \langle \xi(s, \hat{t}) \rangle}{\partial s} \right)^2 \right]^{1/2}. \end{aligned} \tag{1.3}$$

Here, $\underset{\sim}{u}$ indicates a reactant conditioned velocity component, $\langle \xi \rangle$ is the ensemble-averaged flame position and $\hat{t}$ is the phase time (i.e. the time associated with a given point of phase). Related equations for the phase or ensemble-averaged flow dynamics have also been developed for work on the hydrodynamic instability of shear flows in the presence of background turbulence; e.g. see Tammisola & Juniper (2016).

This equation defines the ensemble-averaged turbulent displacement burning speed, $S_{T,D}$, which can be seen by rearranging the above as:

$$S_{T,D}(s, z, \hat{t}) \equiv \frac{\dfrac{\partial \langle \xi(s, \hat{t}) \rangle}{\partial \hat{t}} + \langle \underset{\sim}{u}_s(s, \hat{t}) \rangle \dfrac{\partial \langle \xi(s, \hat{t}) \rangle}{\partial s} - \langle \underset{\sim}{u}_n(s, \hat{t}) \rangle + \langle \underset{\sim}{u}_z(s, \hat{t}) \rangle \dfrac{\partial \langle \xi(s, \hat{t}) \rangle}{\partial z}}{[1 + (\partial \langle \xi(s, \hat{t}) \rangle / \partial z)^2 + (\partial \langle \xi(s, \hat{t}) \rangle / \partial s)^2]^{1/2}}. \tag{1.4}$$

An important finding of this work is that these turbulent effects result in a turbulent flame speed dependence on the ensemble-averaged flame curvature (Shin & Lieuwen 2013). This dependence is analogous to the stretch sensitivity of laminar flames (Wang, Law & Lieuwen 2009). However, this sensitivity is not a manifestation of the instantaneous flames' stretch sensitivity, as these calculations assumed a fixed S_L value, but rather the effect of harmonic wrinkling on the ensemble-averaged flame position. Their results showed that the harmonically modulated turbulent displacement speed can be approximately modelled as:

$$S_{T,D} = S_{T,0}(1 - \sigma_{T,D} \langle C \rangle), \tag{1.5}$$

where $S_{T,0}$ is the uncurved turbulent flame speed, and $\sigma_{T,D}$ is the turbulent Markstein length, reflecting the sensitivity of the flame speed to the ensemble-averaged curvature, $\langle C \rangle$, given by:

$$\langle C \rangle = -\frac{\partial^2 \langle \xi(s, \hat{t}) \rangle / \partial s^2}{[1 + (\partial \langle \xi(s, \hat{t}) \rangle / \partial s)^2]^{3/2}}, \tag{1.6}$$

where the negative sign ensures that negative flame curvatures are regions of the flame concave to the reactants. Further work demonstrated that by including the curvature sensitivity of the ensemble-averaged flame speed, better predictions of the ensemble-averaged flame position, modelled using (1.3) and (1.5), and heat release were achieved (Humphrey *et al.* 2017). A similar flame speed sensitivity to curvature in turbulent, expanding spherical flames has been described by Lipatnikov & Chomiak (2007).

The above review shows that modelling and computational work has been performed on the interactions of harmonic and turbulent disturbances on premixed flames. However, significantly less attention has been given to this topic experimentally. Of course, these interactions are certainly present in the significant number of experimental studies of harmonically forced, turbulent flames (Balachandran *et al.* 2005; Jones *et al.* 2011; Shin *et al.* 2011; Emerson *et al.* 2013), but we are not aware of any prior studies that have explicitly considered them.

There are multiple experimental methods for studying the general problem of flames that are simultaneously disturbed by harmonic and turbulent disturbances. One possibility is to introduce both the turbulent and harmonic components into the velocity forcing field, such as by forcing a speaker with a superposition of narrow- and broadband disturbances. Indeed, this configuration is most representative of what occurs in real applications. For fundamental studies, however, the challenge with interpreting the results of such measurements is that the flame response at a given point is non-local (Lieuwen 2012). That is, the flame response at a given point results from interference between flame wrinkles generated upstream, both at the flame holder and due to the velocity disturbance, and locally excited wrinkles due to the local velocity disturbance (Shin *et al.* 2011). Indeed, our earlier computational studies had originally used this approach but abandoned it for fundamental studies of narrowband–broadband flame disturbance studies, for this very reason.

In contrast, subjecting flames to harmonic oscillations of the flame holder, or otherwise perturbing the flame attachment point, such as described in a few prior studies (Petersen & Emmons 1961; Truffaut & Searby 1999; Kornilov, Schreel & de Goey 2007; Shin & Lieuwen 2013) excites wrinkles at the stabilization point, whose subsequent axial evolution can then be studied. By introducing the harmonic disturbances through the oscillating flame holder, the local flame response becomes much simpler to investigate because it is no longer a convolution of all upstream disturbances (for an isothermal flame), but instead depends only the flame holder oscillation. For non-isothermal flames, however, convecting velocity disturbances are reduced, but not eliminated by using the oscillating flame holder. That is, the density jump across the flame introduces the Darrieus–Landau (D–L) instability and causes the harmonically oscillating flame to introduce harmonic flow disturbances in the reactants and products (Truffaut & Searby 1999); i.e. it is only in the isothermal limit that non-local effects associated with the narrowband disturbances can be eliminated. Nonetheless, the fact that the dominant source of harmonic flame wrinkling can be introduced at a well-defined location is a key motivator for the development of the facility described in this paper.

The rest of this paper is organized as follows. First, a description of the experimental facility is given, describing the burner configuration and the method of harmonic forcing. The following subsections describe the image processing steps necessary for determining the ensemble-averaged flame position, and ensemble-averaged velocity fields. Then, results showing the ensemble-averaged flame position and burning speed are presented in § 3. Lastly, in § 4, we present our conclusions from this work.

2. Experimental methods

2.1. *Experimental set-up*

The experiment is conducted in an atmospheric, premixed methane–air facility. Tests were conducted at an equivalence ratio of 0.95 for the 5 m s^{-1} cases and 0.91 for the 8 m s^{-1} cases. Reactant temperature is approximately 293 K for all cases. A schematic of the experimental set-up is shown in figure 1. The burner test section consists of a circular jet with a throat diameter of 24.1 mm, surrounded by a velocity-matched annular co-flow, with a diameter of 36.3 mm. The mean flow, u_0, is from bottom to top. The bluff body is held approximately 10 mm above the exit plane, bisecting the jet. The bluff body is a 20 AWG (0.81 mm) nichrome wire.

The wire is heated by application of a 6–12 V AC current. The nichrome wire oscillates transverse to the jet flow, driven harmonically at the forcing frequency by two modified 90 W Goldwood speakers (see figure 1). The speakers are connected in parallel to the fixture which holds the oscillating flame holder. The driving signal is created by a function generator and amplified using two linear amplifiers, one for each speaker. The amplitude of flame holder oscillation is approximately 0.33 mm, and varies with frequency by approximately 0.09 mm.

Fuel and air enter the burner at its base through four inlet ports. The flow then passes through a metal screen which mixes the fuel–air mixture and supports a bed of ball-bearings above the screen. After the ball-bearing bed, the fuel–air mix continues through a settling plenum before passing through the variable turbulence generation plates. The turbulence generator consists of two plates with several pie-shaped slots cut through them and is detailed in Marshall *et al.* (2011).

The bottom plate is fixed, while the top plate can rotate over a 28° range. By changing the relative angle between the top and bottom plates, the blockage ratio can be varied from 69 %–97 %. The plate angle is measured from a compass, with an uncertainty of ±0.25°. This turbulence generation system allows the independent variation of the mean flow velocity and turbulence level. For the lowest turbulence case, the plates are removed entirely. However, even in this case the flow has a low turbulence level. After the turbulent generation plates, the flow passes through a contoured nozzle, designed to create a uniform top-hat velocity profile at the plane of the jet exit.

The main air supply is metered using an Aalborg GFC-67, 0–500 l min^{-1} mass flow controller, while the fuel is metered using an Omega FMA-5428, 0–50 l min^{-1} mass flow controller. Co-flow air is metered using an Omega FMA-1843 gas flow meter and manual needle valve. The main air and fuel mass flow controllers are controlled using LabVIEW. The co-flow air is adjusted to match the main jet velocity.

Mie scattering is used both to detect the flame edge and quantify the velocity field using particle image velocimetry (PIV). Images are taken using a Photron Fastcam SA5 high speed video camera with a Nikon Micro-Nikkor $f = 55$ m $f/2.8$ lens, set to a resolution of 768 × 848 pixels for the 200 and 750 Hz cases and 640 × 848

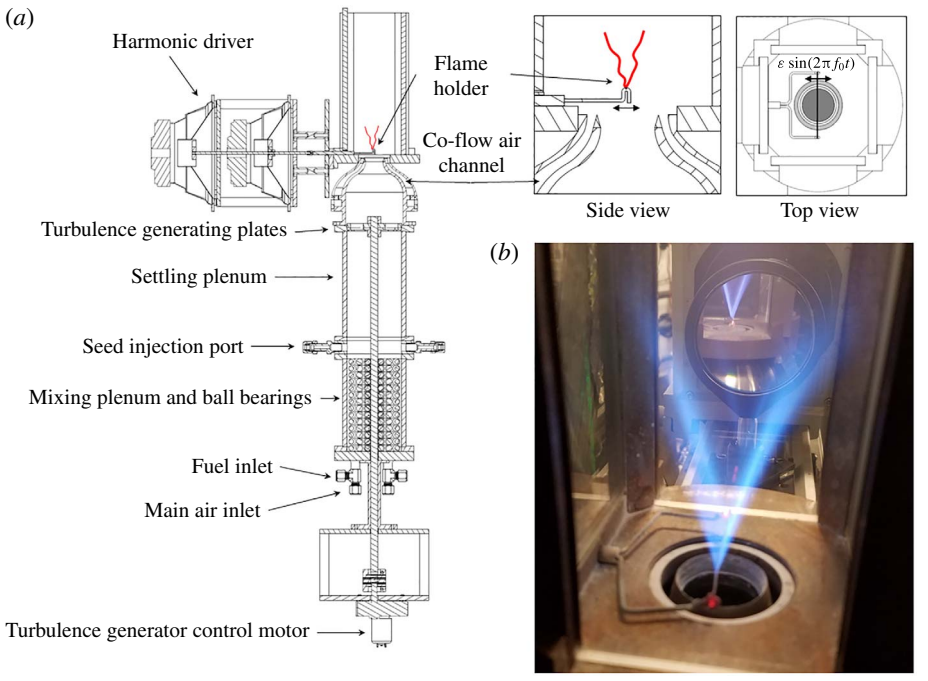

FIGURE 1. (Colour online) (*a*) Schematic of the experimental facility, showing major burner components, and (*b*) an image of the experimental facility in use, showing the V-flame and oscillating flame holder.

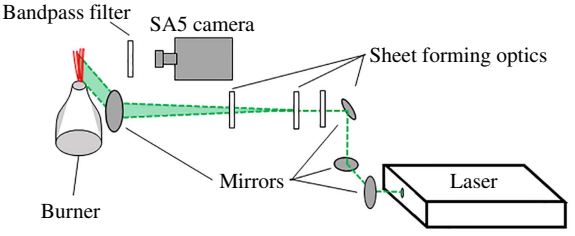

FIGURE 2. (Colour online) Schematic of laser and camera set-up.

pixels for the 1250 Hz case. A bandpass filter is used to minimize off-frequency light. The camera is triggered by a timing box tied to the laser pulse from a dual head, frequency doubled Litron Nd:YLF, 527 nm laser. The laser is formed into a vertical sheet, approximately 6 cm high and 1 mm thick. The laser and optical set-up are shown in figure 2.

Titanium oxide (TiO_2) seed particles, with a nominal diameter of 1 μm are added to the flow by diverting a portion of the main air (prior to mixing with the fuel) through a small cyclone seeder. The seeded flow re-enters the main flow upstream of the settling plenum and prior to the turbulence generator. Cold flow tests show the seed to be well-mixed with the main flow. The co-flow is unseeded.

Three forcing frequencies (200, 750 and 1250 Hz) are investigated at two nominal mean, axial flow velocities (5 m s^{-1} and 8 m s^{-1}), denoted as $U_{x,0}$, and four turbulence intensities each ($u'/u_{x,0} \approx 8\,\%$–$32\,\%$), where u' is the root mean square of

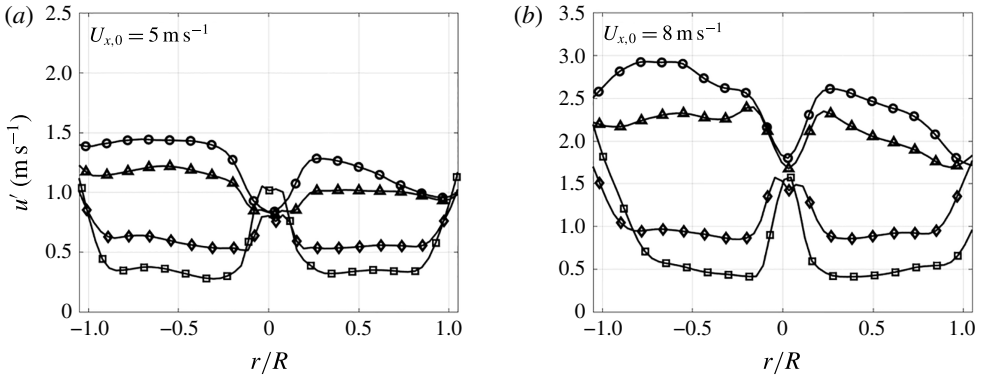

FIGURE 3. Radial dependence of the turbulence intensity at four different turbulence intensities for the nominally 5 m s^{-1} cases (*a*), and 8 m s^{-1} cases (*b*) at a cut 1.5 mm above the flame holder location.

the turbulent velocity fluctuations, and $u_{x,0}$ is the mean measured axial flow velocity. For the 200 Hz cases, pairs of images are recorded at 2000 Hz. For the 750 and 1250 Hz cases, a sequence of images is taken at 7500 and 12 500 Hz, respectively. These acquisition rates result in 10 samples per forcing cycle for all conditions and, by virtue of being a nearly exact integer multiple of the forcing frequency, virtually eliminate spectral leakage bias errors in spectral estimation. The total number of image pairs is 8790, 17 580 and 21 095, for the 200, 750 and 1250 Hz cases, respectively.

PIV processing is accomplished with LaVision DaVis PIV software (LaVision 2016), using a multipass algorithm. The first pass uses a 48 × 48-pixel interrogation window, with 25 % overlap between windows, while two subsequent passes use an 8 × 8-pixel window, with a 25 % overlap. This yields a resolution 6 pixels (∼0.46 mm) between vectors. However, note that due to the window overlap, adjacent velocity vectors are not completely independent. The uncertainty of these measurements and calculations is discussed in § 2.2.3.

Figure 3 plots the radial dependence of the root mean square of the turbulent fluctuations, u', at a cut 1.5 mm above the flame holder location for the 750 Hz cases. Similar results are observed for the 200 Hz and 1250 Hz cases. For the lower turbulence levels, u' is approximately constant across the jet except near the oscillating flame holder, where large deviations are observed, which are due to the flame holder and flame movement. The spatial variation in u' near the edge of the jet is due to intermittency between the unseeded co-flow and main jet, and does not occur at higher turbulence due to the increased jet spreading which results in better seeding in this region. The values of u' quoted later are obtained separately from the left and right sides of the centreline, as there is some asymmetry in the highest turbulence intensity cases.

The integral time scale was estimated by computing the autocorrelation based on PIV data. The estimated autocorrelation results were fit with an exponential function, $\rho(\tau) = a\exp(-bt) + (1-a)\exp(-ct)$. The integral time scale is computed by taking the integral of the fit equation, i.e. $\tau_{int} = \int_0^\infty \rho(\tau)\,\mathrm{d}\tau$. Using this method, the estimated integral time, $\tau_{int}U_{x,0}/D = 0.19$ and varies by $\sim \pm 0.09$.

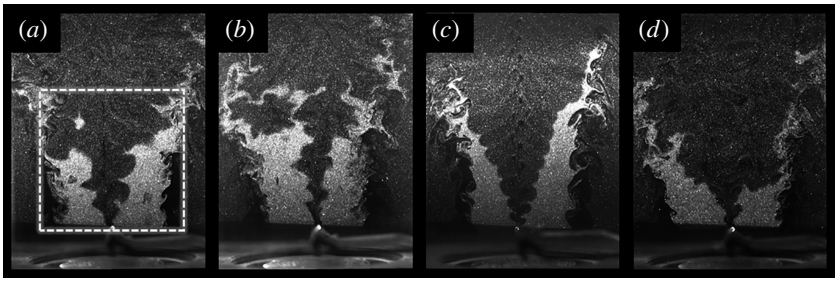

FIGURE 4. Four representative instantaneous flame images, at (*a*) $f_0 = 750$ Hz, $u_{x,0} = 4.2$ m s^{-1}, $u'/u_{x,0} = 26.8\,\%$, (*b*) $f_0 = 750$ Hz, $u_{x,0} = 7.1$ m s^{-1}, $u'/u_{x,0} = 25.5\,\%$, (*c*) $f_0 = 1250$ Hz, $u_{x,0} = 4.2$ m s^{-1}, $u'/u_{x,0} = 12.2\,\%$, (*c*) $f_0 = 1250$ Hz, $u_{x,0} = 6.7$ m s^{-1}, $u'/u_{x,0} = 28.0\,\%$. Image (*a*) shows the cropped region.

2.2. *Image and data processing*

2.2.1. *Image processing procedure*

This section details the steps used to extract ensemble-averaged flame edge and flow field data. The raw images collected during the experimental run are first de-warped using LaVision's DaVis PIV processing software (LaVision 2016). This step corrects image distortion due to the presence of the quartz window and provides physical reference coordinates for the images. Figure 4 shows four representative images of the flame at different conditions, at this stage of processing.

If necessary, the strength of unwanted reflections is reduced using a sliding minimum subtraction method. This algorithm subtracts a weighted minimum intensity value (determined over a set number of images at a given point of phase) at each pixel, effectively removing persistently bright pixels. However, for most cases this step was not required. Next, axial (i.e. flow direction) variation in the image brightness, resulting from laser sheet intensity variation, is normalized. This normalization uses the average brightness of a region with recirculating seed and illuminated by the laser, but beyond the edge of the jet as a reference. The normalization is accomplished by dividing each row in the image by the corresponding row in the intensity reference multiplied by a weighting factor. After normalizing the images, they are filtered using a Gaussian filter, which removes high frequency noise, and then filtered with an edge-preserving bilateral filter.

The images are cropped to a region containing the flame, reactants, and the region downstream of the co-flow, as the flame expands into this region due to flow divergence around the flame, as shown in figures 4 and 5. The cropped images are binarized using a weighted threshold based on Otsu's method (Otsu 1979). This produces a series of instantaneous, binary flame images, such as shown in figure 5.

In order to determine the ensemble-averaged flame edge, the set of instantaneous binary images at a given phase in the forcing cycle are averaged together. This produces an ensemble-averaged progress variable field, which varies from unity in the reactants to zero in the products. The ensemble-averaged flame edge associated with some reference progress variable contour is then extracted, as shown in the fourth image in figure 5. Note that the coherent harmonic wrinkle, initially obscured by the turbulent fluctuations, becomes evident after ensemble averaging. The result of these processing steps is the physical location of the ensemble-averaged flame edge, at each phase in the forcing cycle. Two videos of ensemble-averaged flames are included

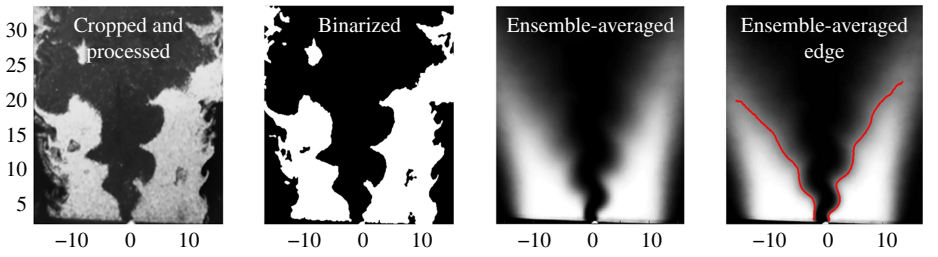

FIGURE 5. (Colour online) Identification of ensemble-averaged flame edges from instantaneous flame images, at $u_{x,0} = 4.2$ m s^{-1}, $u'/u_{x,0} = 26.5\,\%$, and $f_0 = 750$ Hz. Ensemble-averaged edge shown at $\bar{C} = 0.5$. Dimensions shown are in mm.

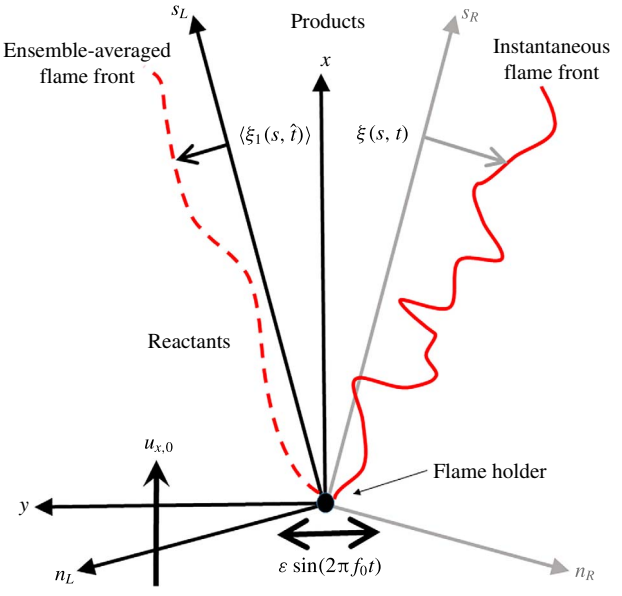

FIGURE 6. (Colour online) Schematic of the coordinate system, ensemble-averaged turbulent flame (dashed), and instantaneous flame (solid). The excitation amplitude is ε, $2\pi f_0$ is the radial driving frequency.

in the supplemental, online material available at https://doi.org/10.1017/jfm.2017.728. Note that because flame locations are determined by averaging a series of binary images, the resulting flame positions reflect the median location of the flames rather than the arithmetic mean of the flame locations. See Shin & Lieuwen (2013) for further discussion of this difference.

2.2.2. *Ensemble-averaged flame and flow field*

Figure 6 shows a simple schematic of the flame geometry, and the coordinate systems used in defining the ensemble-averaged flame wrinkles. The s-coordinate is defined as the mean flame position. Although the mean flame position is not exactly a straight line, it is nearly so: linear regressions on the full mean flame yield an average correlation coefficient (R^2) value of 0.97, with the lowest observed $R^2 = 0.91$.

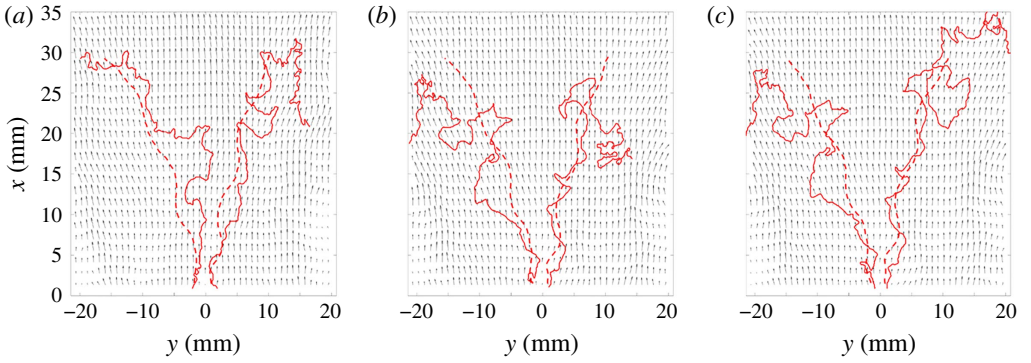

FIGURE 7. (Colour online) Representative instantaneous flow field and flame edge (solid) and ensemble-averaged flame edge (dashed), at $u_{x,0} = 7.2$ m s^{-1}, $u'/u_{x,0} = 25.6\,\%$ and $f_0 =$ 750 Hz. Phase increases from left to right, in increments of $\Delta\hat{t}/T = 0.10$, where T is the cycle period.

In order to determine the fluctuating, ensemble-averaged flame position, and reduce the noise inherent in the experimental data, several processing steps are required. These processing steps are needed because the edge data extracted from the ensemble-averaged progress variable fields is subject to spatial aliasing. In order to remove noise in the extracted data, the ensemble-averaged flame edge is fit with a smoothing spline curve. Only minimal smoothing is necessary, and the interpolated flame edges fit the original edge data well, with $R^2 > 0.99$ for all cases.

The ensemble-averaged, fluctuating flame position as a function of the s coordinate, $\xi_1(s, \hat{t})$, is extracted from the ensemble-averaged flame edge data (see figure 6) by determining the perpendicular distance from the mean flame to the ensemble-averaged flame (using a normal vector defined from a linear regression with a sliding stencil on the mean flame), at each s location on the mean flame, and at each phase. The flame position is defined as positive towards the reactants, regardless of whether it is the left or right flame edge, as shown in figure 6. The result of these processing steps are ensemble-averaged, fluctuating flame positions, as shown in figure 9, which is discussed further in the next section. While the instantaneous flame may be highly corrugated, the ensemble-averaged flame is relatively smooth. In fact, the ensemble-averaged flame actually becomes smoother with increasing turbulence intensity due to the kinematic restoration effect discussed earlier, even while the instantaneous flame becomes more wrinkled.

The velocity field is determined using PIV measurements, as described previously in § 2.2.1. Representative instantaneous flow results, with the instantaneous and ensemble-averaged flame position are shown in figure 7. The velocity fields are ensemble averaged by averaging the instantaneous, reactant-conditioned, velocity fields at a given phase of the forcing cycle. Reactant conditioning is carried out by only including velocity values from the reactants, upstream of the instantaneous flame. This averaging procedure produces ensemble-averaged, reactant-conditioned velocity fields, u, which are a function of spatial location and phase.

Although the present analysis does not rule out effects of out of plane flame motion – which may alter the curvature and displacement speed statistics of instantaneous, local flame measurements (Kerl *et al.* 2013) – note that because the $S_{T,D}$ definition utilizes ensemble-averaged flame and flow fields, the results are

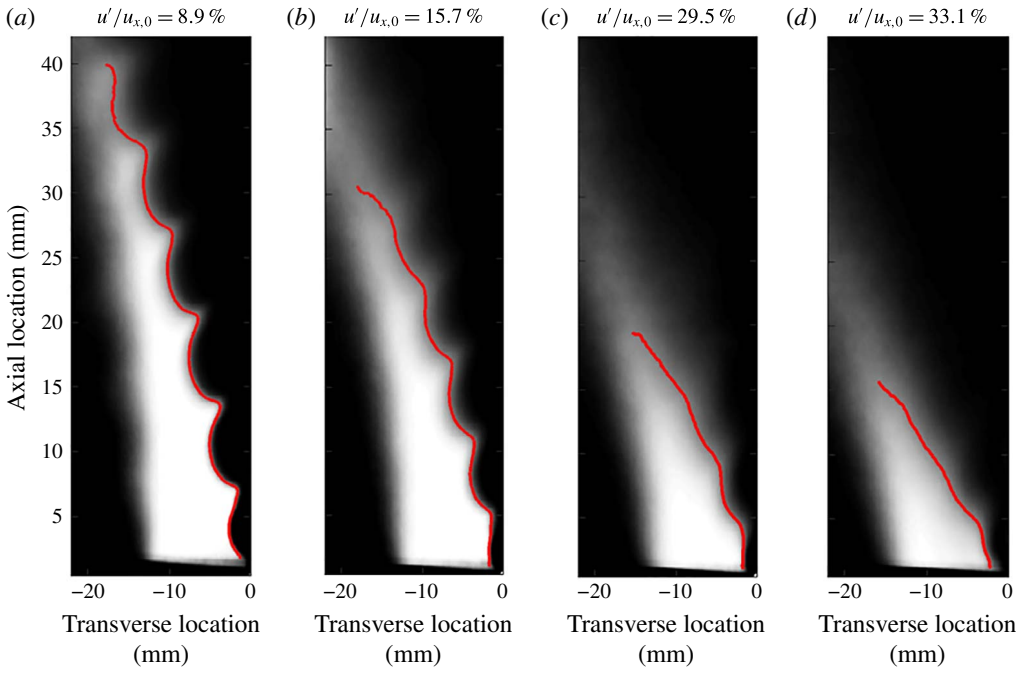

FIGURE 8. (Colour online) Ensemble-averaged flame at $\bar{C} = 0.5$ and progress variable field showing the decrease in wrinkling amplitude and degree of cusping with increasing turbulence intensity, $f_0 = 750$ Hz, $u_{x,0} = 4.9$, 4.7, 4.1 and 3.8 m s^{-1}, from (*a*) to (*d*).

effectively two-dimensional. That is, the ensemble-averaged displacement speed being measured here is effectively a two-dimensional quantity.

In addition to the ensemble-averaged velocity field, calculation of the ensemble-averaged turbulent burning speed, $S_{T,D}$, (defined in (1.4)) requires the first derivative of the flame with respect to s. This is computed by fitting a spline to the ensemble-averaged flame fluctuation. The first (and second) derivatives can then be calculated from the spline fit. Note that the second derivative is required for calculation of the ensemble-averaged flame curvature. This fitting procedure is used in order to minimize the amplification of noise which otherwise occurs when finding finite difference approximations to derivatives. Derivatives in the phase domain are computed using a weighted essentially non-oscillatory (WENO) derivative algorithm (Jiang & Peng 2000). This is necessary because the change of flame position in time can be discontinuous as a result of strong cusp formation. These strong cusps are particularly evident at the lowest turbulence intensities, while increasing turbulence intensity significantly decreases their magnitude, as shown in figure 8. The WENO derivative is designed to accurately measure the derivative of a function with such discontinuous derivatives.

2.2.3. *Uncertainty analysis*

Uncertainty in flame position is determined by comparison of raw, instantaneous flame images with the algorithmically determined instantaneous flame edge. The thickness of the flame edge is manually adjusted until it overlaps the apparent flame edge based on the raw image. The thickness is recorded, and this procedure is

repeated for 55 images for each data set. A one-sided, 95 % confidence interval is calculated for each set of thickness values, and this measurement is taken to be the uncertainty in instantaneous flame position.

In order to determine the uncertainty of the calculated ensemble-averaged turbulent flame speeds, the ensemble-averaged flame edge uncertainty is calculated from the instantaneous flame edge uncertainty, using standard propagation of uncertainty techniques (Wheeler & Ganji 1996). However, because of the complexity of the processing algorithms used to extract the ensemble-averaged flame and flow fields used in the calculation of the ensemble-averaged turbulent burning speed, $S_{T,D}$, a Monte Carlo approach is adopted in order to determine flame speed uncertainty. This is accomplished by first creating a synthetic progress variable field which is qualitatively similar to the actual data, but based on a known analytical function. The analytical function has the same number of phase points, and the same approximate shape, wrinkle magnitude and convection speed as the experimental data. Gaussian noise with a specified mean and standard deviation, determined from the ensemble-averaged flame position data (discussed above), is introduced. Similarly, synthetic velocity fields with the same mean axial velocity are created. Again, noise is introduced in these data based on the mean axial velocity, frame position, time delay between PIV image pairs, number of velocity data points included in each phase average, pixel size and uncertainty in the calibration plate used for PIV analysis, as discussed further below.

The synthetic data is processed using the same algorithm as that used for the actual experimental data. Uncertainty is determined by comparison of relevant quantities (i.e. derivatives of flame position and velocity) with the known, analytical function on which the synthetic data are based. For each quantity, a one-sided, 95 % confidence interval is determined and this value is used to find the relative uncertainty in a given quantity. Finally, the uncertainty of an actual ensemble-averaged flame speed data point is determined using standard error propagation techniques, which provides final uncertainty estimates that vary depending on the magnitude of measured quantities (i.e. an uncertainty is found for each data point). Uncertainties in averaged quantities are again determined using standard uncertainty propagation techniques.

The turbulent Markstein length, $\sigma_{T,D}$, and uncurved turbulent flame speed, $S_{T,0}$, are calculated from the slope and intercept of an orthogonal regression between the $S_{T,D}$ and $\langle C \rangle$ values, as discussed in § 3.1. In order to characterize the uncertainty in $\sigma_{T,D}$ and $S_{T,0}$ a Monte Carlo approach is also used. Synthetic data is created by drawing from a normal distribution with a mean equal to the calculated experimental data value and a standard deviation equal to one half the same data point's uncertainty. These synthetic data are generated in each flame curvature bin, as shown in figure 17. Estimates of $\sigma_{T,D}$ and $S_{T,0}$ are determined from 1000 independently generated realizations. A 95 %, two-sided confidence interval based on these 1000 synthetic values of $\sigma_{T,D}$ and $S_{T,0}$ provides the uncertainty estimate.

Uncertainty estimates of the instantaneous PIV flow field measurements are based on four factors: out of plane particle movement, particle aliasing due to pixel resolution, calibration error due to pixel resolution and the manufacturing tolerance of the calibration plate. The effect of out of plane particle movement increases from zero at the centre of the image to approximately 20 % at the edges of the image. The uncertainty in the particle position due to finite resolution is estimated as 10 % of the pixel size. Similarly, the uncertainty of the calibration due to finite pixel resolution is estimated as 10 % of the pixel size. The manufacturing tolerance of the calibration plate is 0.02 mm. The uncertainties resulting from these factors are treated additively.

Because these uncertainty estimates depend both on the mean flow velocity and the time delay between images, the uncertainty due to a given factor and the overall uncertainty vary from case to case. Uncertainties due to out of plane motion and particle location are treated as random uncertainties, while the uncertainties resulting from calibration error are treated as bias errors. The resulting PIV uncertainty varies significantly with position for a given case (due to out of plane particle motion) and between cases, due to differences in mean velocity and different time delays between image pairs.

The largest uncertainties in instantaneous, ensemble-averaged, and time-averaged velocities are approximately 17 %, 6 % and 5 %, respectively. The largest uncertainty of the ensemble-averaged velocity fields used for calculation of the ensemble-averaged turbulent displacement speed is approximately 6 %.

3. Results and discussion

This section presents results for the ensemble-averaged flame position and $S_{T,D}$. Figure 9 shows the ensemble-averaged flame position fluctuation at two forcing frequencies and four turbulence intensities. Each line is the ensemble-averaged flame edge at given phase. Note that harmonic wrinkling is not necessarily evident on the instantaneous flame, but can be seen much more readily by the ensemble-averaging process. Clear harmonic wrinkling of the flame is observed in all cases. In addition, the downstream convection of these flame wrinkles is also evident by the axial translation of the wrinkles at subsequent phases.

At the lowest turbulence intensity and a forcing frequency of 750 Hz, approximately five full spatial periods of oscillation are present on the flame, while at 1250 Hz, there are approximately eight full periods of oscillation, reflecting the reduced convective length scale at 1250 Hz. Representative results from the 750 and 1250 Hz cases are examined in the following discussion and results.

As introduced in § 2.2.2, the flame positions are the median rather than the arithmetic mean of the flame position. This is most pronounced in the low turbulence intensity cases figure 9(*a*,*e*), where the flame is clearly asymmetrically distributed around the zero location. This effect decreases with increasing turbulence due to the decrease in the magnitude of the flame position fluctuations, as the median does not reflect the magnitude of outlying events.

One of the most prominent observations from these data is the smoothing effect of turbulent fluctuations on the harmonic flame wrinkle. In the low turbulence cases (figure 9*a*,*e*) the harmonic flame wrinkles persist beyond the experimentally observable window, while for the high turbulence intensity cases (figure 9*c*,*d*,*g*,*h*) the harmonic wrinkles are damped out to within the measurement tolerance, after approximately 10–20 mm downstream from the flame holder. This smoothing effect increases monotonically with turbulence intensity. This result is consistent with conclusions reached in prior isothermal computations from Shin & Lieuwen (2013) and Hemchandra *et al.* (2007). These data are the first measurements we are aware of demonstrating this effect. Thus, these results clearly show that turbulent flow disturbances dissipate the magnitude of wrinkles introduced on the flame by acoustic disturbances and/or quasi-coherent large-scale vortical structures.

Isothermal calculations and modelling results suggest that the wrinkle amplitude should decay exponentially with distance downstream. These data clearly show that this is not the case. Rather, the growth/decay in flame wrinkle amplitude is non-monotonic for the two lower turbulence cases at 750 Hz, and the lowest

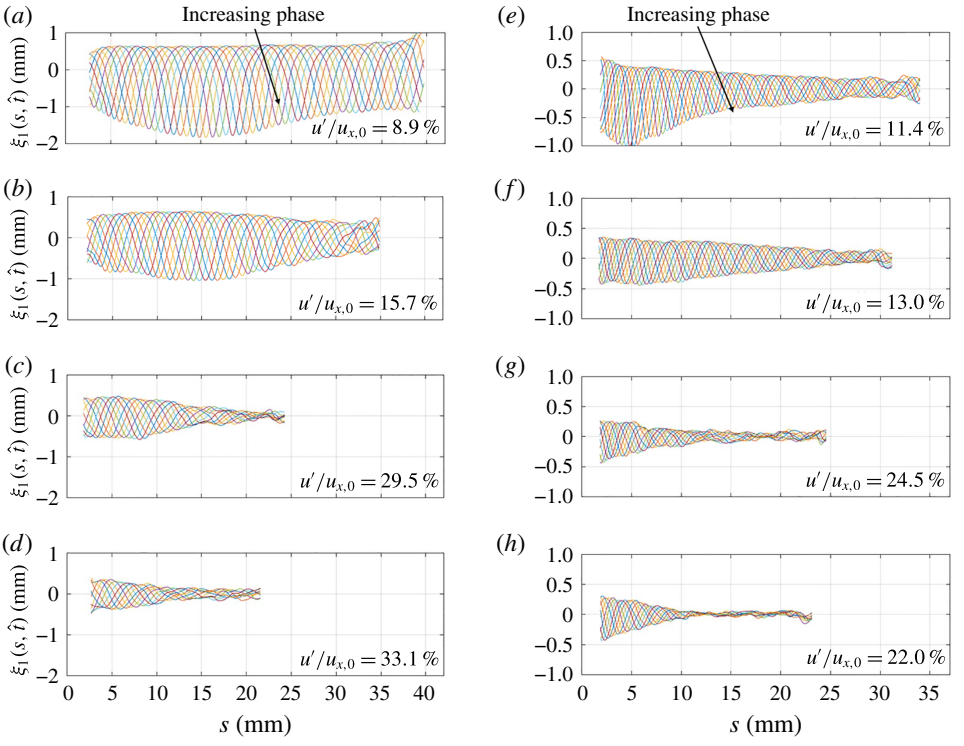

FIGURE 9. (Colour online) Ensemble-averaged flame position fluctuations with increasing turbulence intensity at $f_0 = 750$ Hz, $u_{x,0} = 4.9$, 4.7, 4.1 and 3.8 m s^{-1} (*a–d*) and $f_0 = 1250$ Hz, $u_{x,0} = 4.5$, 4.6, 4.3 and 4.4 m s^{-1} (*e–h*).

turbulence case at 1250 Hz. For the two lowest turbulence intensities, flame wrinkle amplitude first grows up to an axial position of ∼17 mm, in figure 9(*a*) before decreasing further downstream. This non-monotonic behaviour is likely due to gas expansion effects which induce phase-coherent velocity disturbances, as discussed next.

Detailed analysis of figure 9 shows the effect of an additional convecting disturbance, for the low and moderate turbulence intensity cases. This disturbance likely results from vortex shedding from the flame and the D–L flame instability. Note that a significant difference between the current work and the previous computational studies is that only an isothermal flame was considered by Shin & Lieuwen (2013) and Hemchandra *et al.* (2007), effectively removing the influence of the flame on the flow field. An important effect of heat release (i.e. non-isothermal effects) is to cause the flame to disturb the approach flow, or stated alternatively, to introduce the D–L instability. These gas expansion effects cause the flame wrinkles to modulate the approach flow velocity, also introducing an additional source for coherent wrinkles on the flame.

This coherent velocity disturbance can be seen clearly in the data in figure 10(*a*), which shows the normal component of the reactant conditioned, ensemble-averaged velocity. The figure shows a propagating disturbance on the velocity beyond about $s = 5$ mm. Again, this velocity disturbance is not directly excited in the experiment (only flame base motion and turbulent flow disturbances are directly excited) – rather,

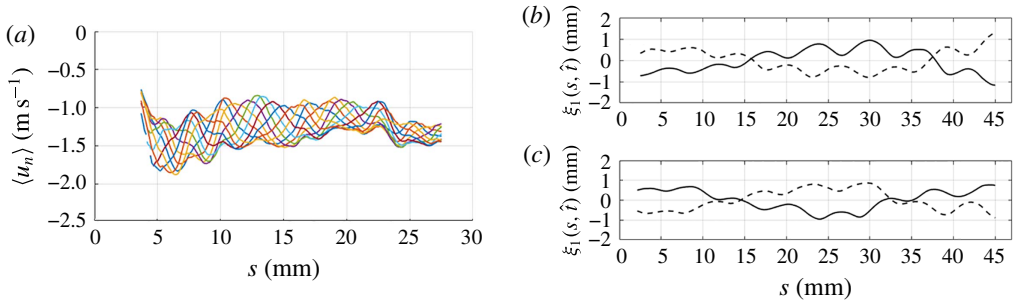

FIGURE 10. (Colour online) (*a*) Ensemble-averaged normal velocity along the mean flame position (average over all phases), at $f_0 = 750$ Hz, $u_{x,0} = 4.8$ m s^{-1}, $u'/u_{x,0} = 9.3\,\%$. (*b*,*c*) Ensemble average flame position, showing the effect of the convecting vortex at two points of phase, $\Delta\hat{t}/T = 0$ (solid) and $\Delta\hat{t}/T = 0.5$ (dashed) for (*b*) $f_0 = 200$ Hz, $u_{x,0} = 8.1$ m s^{-1}, $u'/u_{x,0} = 8.8\,\%$, and (*c*) $f_0 = 200$ Hz, $u_{x,0} = 8.1$ m s^{-1}, $u'/u_{x,0} = 8.4\,\%$.

it is an indirect effect due to vortex shedding and gas expansion-induced motion. This harmonic modulation of the disturbance velocity provides an indicator of how important non-isothermal effects and the D–L instability are in understanding these interactions.

For the result in figure 10(*a*), it shows that the induced disturbance in velocity is about 18 % of the mean velocity. This convecting flow disturbance can also be seen in figure 10(*b*,*c*), which plots the ensemble-averaged flame at two points of phase at the lowest frequency for which data were obtained. For this low frequency ($f_0 = 200$ Hz) case, only approximately three quarters of the convective wavelength due to the harmonic flame holder movement appears on the flame, enabling more clear separation in scales of the flame wrinkling induced by flame holder motion and convecting velocity disturbances. The smaller-scale undulations are the result of a velocity disturbance.

3.1. *Turbulent ensemble-averaged burning velocity*

Although the flame position is important in its own right, the ensemble-averaged burning speed, $S_{T,D}$, provides insight into how it is temporally modulated by the harmonic disturbances. Values of $S_{T,D}$ are determined from the ensemble-averaged velocity and flame edge data, using (1.4). As discussed above, the ensemble-averaged flame develops small-scale wrinkles which are not directly due to harmonic flame holder motion, and these regions are not included in the flame speed calculations as they add significant noise to the calculation of derivatives. For example, in figure 9(*b*) the included region corresponds to $s = 4$–30 mm.

Note that $S_{T,D}$ is a function of both time (or, more precisely, the phase) and space, as opposed to the more familiar turbulent displacement speed which is taken as a time average and, consequently, is only a function of space. The average of $S_{T,D}$ over all phases, denoted as $\bar{S}_{T,D}$, provides a measure of the spatial dependence of $S_{T,D}$, as shown in figure 11. Note that $\bar{S}_{T,D}$ is a function of both harmonic disturbance amplitude and turbulence intensity, so all results are shown for constant $\varepsilon \approx 0.32$ mm (figure 11). The laminar flame speed, $S_{L,0}$, is calculated as 0.37 m s^{-1} for the 5 m s^{-1} cases and 0.34 m s^{-1} for the 8 m s^{-1} cases, based on a Chemkin (Kee *et al.* 2011) PREMIX calculation using the GRI-Mech 3.0 mechanism (Smith *et al.* 0000).

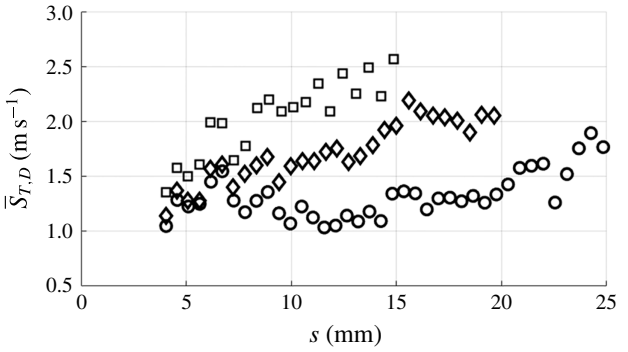

FIGURE 11. Ensemble-averaged turbulent burning speed, averaged over all phases, $\bar{S}_{T,D}$, at $f_0 = 750$ Hz, $u_{x,0} = 4.6$, 4.3 and 4.4 m s^{-1} and $u'/u_{x,0} = 14.6$, 24.4 and 26.4 %, for circles, diamonds and squares, respectively.

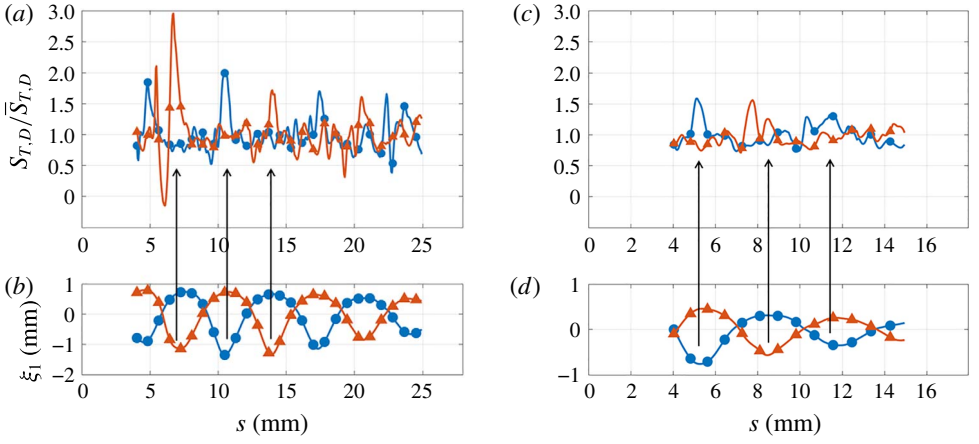

FIGURE 12. (Colour online) Ensemble-averaged turbulent displacement speed (*a*,*c*) and flame fluctuation (*b*,*d*) as a function of the flame coordinate, at $f_0 = 750$ Hz, (*a*,*b*) $u_{x,0} = 4.6$ m s^{-1}, $u'/u_{x,0} = 14.6$ %, (*c*,*d*), $u_{x,0} = 4.4$ m s^{-1}, $u'/u_{x,0} = 26.4$ % at two phases, $\Delta\hat{t}/T = 0$ (circles) and $\Delta\hat{t}/T = 0.5$ (triangles).

The mean ensemble-averaged turbulent burning speed increases in an approximately monotonic fashion with increasing downstream distance. This is a familiar result in anchored flames (Lipatnikov 2012). In general, $\bar{S}_{T,D}$ also increases with increasing turbulence intensity. The value of $\bar{S}_{T,D}$ at the higher turbulence intensities is approximately 1.5–2.3 times greater than at the lowest turbulence intensities, for both forcing frequencies.

Consider next the axial dependence of the phase-dependent burning speed, $S_{T,D}$. Both the 750 Hz (figure 12) and 1250 Hz (figure 13) cases show significant variations in $S_{T,D}$ with the flame coordinate. Several trends are evident – of particular interest are changes in $S_{T,D}$ which correspond with the curvature of the ensemble-averaged flame. For instance, figure 12(*a*) shows a series of peaks in the flame speed with the magnitude of the peaks diminishing with the s coordinate. In the flame wrinkle plot (figure 12*b*), it can be seen that these peaks generally correspond to regions of

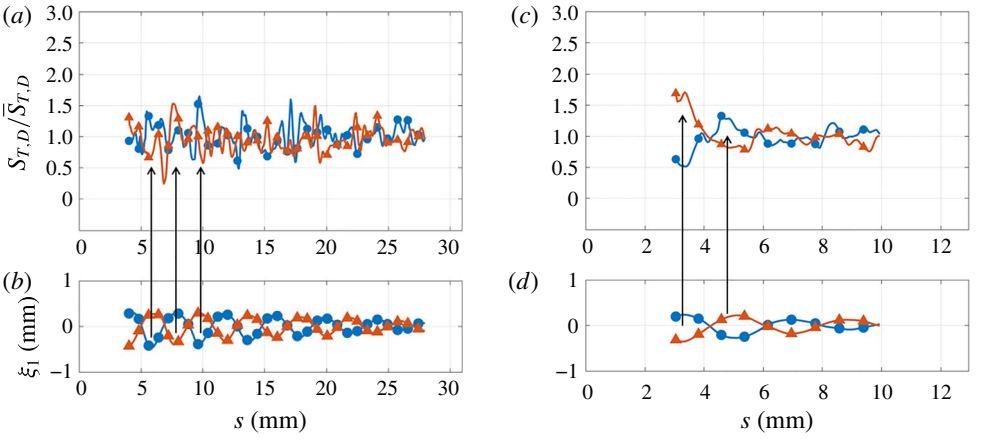

FIGURE 13. (Colour online) Ensemble-averaged turbulent displacement speed (*a*,*c*) and flame fluctuation (*b*,*d*) as a function of the flame coordinate, at $f_0 = 1250$ Hz, (*a*,*b*) $u_{x,0} = 4.6$ m s^{-1}, $u'/u_{x,0} = 13.0\,\%$, (*c*,*d*) $u_{x,0} = 4.4$ m s^{-1}, $u'/u_{x,0} = 22.0\,\%$, at two phases, $\Delta\hat{t}/T = 0$ (circles) and $\Delta\hat{t}/T = 0.5$ (triangles).

negative flame curvature. For example, consider figure 12(*a*) at $s \approx 7$, 11, 13, 17 and 21 mm. The maxima in flame speed is also noticeable for the higher turbulence intensity figure 12(*c*). However, the maxima are not as sharp, a reflection of the fact that the ensemble-averaged flame is smoother for the higher turbulence intensity case. In other words, $\langle C \rangle$ varies more smoothly at higher turbulence (at increasing s) than at the lower turbulence intensity case, where the flame is composed of broad regions of positive curvature, punctuated by relatively narrow regions of strongly negative curvature.

This same modulation of $S_{T,D}$ is also clearly evident in figure 13, which plots the ensemble-averaged turbulent displacement speed for a 1250 Hz case. Again, there is a distinct correspondence between points of negative curvature and local peaks in the ensemble-averaged turbulent flame speed, for both points of phase shown. For the lower turbulence intensity case (figure 13*a*,*b*) the peaks are sharper than for the higher turbulence intensity case (figure 13*c*,*d*). Again, increased turbulence intensity smooths the flame wrinkles, decreasing the magnitude of ensemble-averaged flame curvature. Thus, the areas of increased flame speed are also broadened and of lower magnitude. Like the 750 Hz cases (figure 12) the 1250 Hz cases shown in figure 13 also demonstrate diminishing flame speed modulation with downstream distance. As the flame wrinkles decay, so too do the modulations in ensemble-averaged turbulent flame speed. Additionally, the magnitude of flame speed modulation appears reduced at 1250 Hz as compared to the 750 Hz case, due to the somewhat reduced flame wrinkle size, as seen in figure 9.

To further examine the modulation of $S_{T,D}$, figure 14 shows a probability density function (PDF) plot of the normalized ensemble-averaged displacement speed plotted against the normalized ensemble-averaged curvature. The best fit line in figure 14 and those used in determining the turbulent Markstein lengths shown later are determined by orthogonal linear regression (i.e. a procedure that minimizes the orthogonal distance from the best fit line to the data, rather than minimizing either the x or the y distance). The orthogonal linear regression is the appropriate regression tool

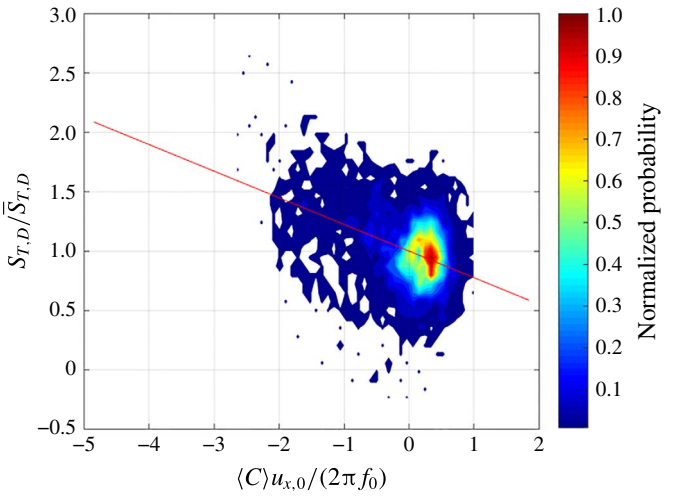

FIGURE 14. (Colour online) PDF plot of the ensemble-averaged turbulent displacement speed versus normalized ensemble-averaged flame curvature at $f_0 = 750$ Hz, $u_{x,0} = 4.7$ m s^{-1}, $u'/u_{x,0} = 15.7\,\%$. The red line is determined by orthogonal linear regression.

when there is uncertainty in both the regression variable and the regressor (Ling *et al.* 2007)), in this case the experimentally determined ensemble-averaged flame curvature.

Figure 14 shows that $S_{T,D}$ correlates with $\langle C\rangle$. Specifically, $S_{T,D}$ increases with negative ensemble-averaged flame curvature. This point was previously inferred from the analysis of figures 12 and 13, but can be seen more directly here.

However, while figure 14 provides evidence for this relationship, the relationship between $S_{T,D}$ and $\langle C\rangle$ cannot be determined using a straightforward regression analysis, as this leads to significant bias errors because the data is not uniformly distributed in curvature space. Figure 14 clearly shows a clustering of data for ensemble-averaged curvatures between zero and unity, which has the effect of biasing any regression between the two variables towards values in a relatively narrow, positive curvature range. This analysis is concerned with the effect of flame curvature not only at these most probable, positive curvature locations but also for relatively improbable events at large negative flame curvature. Therefore, an additional processing step is utilized to minimize bias error effects due to the non-uniform sampling in curvature space. First, the data is divided into bins for sub-ranges of curvature values. Then, a conditional median value for $S_{T,D}$ is determined in each curvature bin where there are at least five data points. The median, rather than a mean, is used so that the value for a given bin is not skewed by outlying data points. Several representative results of this procedure are shown in figures 15 and 17.

These data are the most significant result from this study, and clearly show the relationship between curvature and turbulent displacement speed. In particular, they show the approximately linear rise in $S_{T,D}$ with decreasing ensemble-averaged curvature. Note the use of a slightly different non-dimensionalization for curvature in figure 15(*b*). $S_{T,D}$ and $S_{T,eff}$ are both defined from (1.4), however, the $S_{T,eff}$ calculation used an ensemble-averaged flame based on the mean, rather than the median, flame location. Figure 15(*a*) also shows that, for this case, the uncurved ensemble-averaged turbulent displacement speed, $S_{T,0}$, (i.e. the intercept of the regression line at zero curvature) and the slope of the regression demonstrate similar

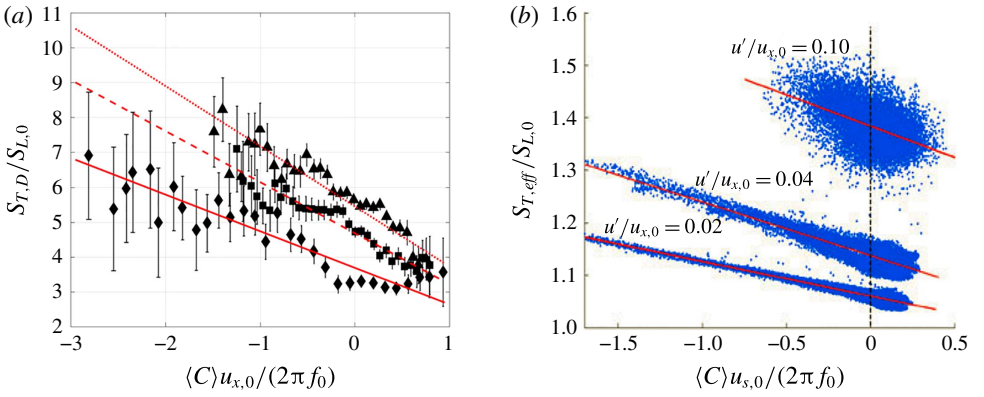

FIGURE 15. (Colour online) (*a*) Dependence of the ensemble-averaged turbulent displacement speed upon ensemble-averaged curvature at $f_0 = 750$ Hz, $U_{x,0} = 5.0$ m s^{-1}, $\bar{C} = 0.5$, for three turbulence intensities, $u_{x,0} = 4.7$ m s^{-1}, $u'/u_{x,0} = 15.7\,\%$ (solid line, diamonds), $u_{x,0} = 4.1$ m s^{-1}, $u'/u_{x,0} = 29.5\,\%$ (dashed line, squares) and $u_{x,0} = 3.8$ m s^{-1}, $u'/u_{x,0} = 33.1\,\%$ (dotted line, triangles). (*b*) Numerical results reproduced from Shin & Lieuwen (2013).

sensitivities to increasing turbulence. That is, the uncurved turbulent displacement speed increases with increasing turbulence, and the sensitivity of the flame speed to curvature (as characterized by the slope of the regression line) increases. However, in general the dependence of slope and intercept is not a monotonic function of turbulence intensity, as discussed later. For reference, figure 15(*b*) reproduces a result from Shin & Lieuwen (2013), which shows a scatterplot of calculated $S_{T,D}$ values (i.e. the data are not averaged in curvature bins as in figure 15*a*), also demonstrating an approximately linear relationship between the ensemble-averaged flame curvature and flame speed. Both results are consistent with the closure in (1.5), previously proposed by Shin & Lieuwen (2013).

The dependence of $S_{T,D}$ on $\langle C\rangle$ shown in figures 15 and 17 results from the interaction between the large-scale, narrowband disturbances due to the harmonic forcing and the small-scale, broadband disturbances due to turbulence. Figure 16 illustrates this effect. For a flame with coherent negative curvature, as shown on the right-hand side of the figure, the distance between opposing flame surfaces will on average be decreased, particularly at the trailing edge of the flame (Shin & Lieuwen 2013). In turn, this increases the rate at which opposing faces will interact and annihilate one another through kinematic restoration (i.e. the propagation of the flame normal to itself). The net result is that the average flame surface propagates further in the negatively curved case than for positive or neutral curvature over a given time increment.

Similar relationships between $S_{T,D}$ and $\langle C\rangle$ were observed for all 750 and 1250 Hz cases, as illustrated in figure 17. In these results, we normalize $S_{T,D}$ by the local average value, $\bar{S}_{T,D}$, and denote this quantity as S_T, which somewhat reduces the sensitivity of the plots to turbulence intensity and helps identify the spatio-temporal modulation of the phase-dependent flame speed. Figure 17(*c*) illustrates the relationship of the normalized uncurved turbulent flame speed values, $S_{T,0}$, and the 'normalized turbulent Markstein length', $\mathcal{M}_{T,D}$ to the intercept and slope of the regression line. Note that while $\mathcal{M}_{T,D}$ describes the same fundamental

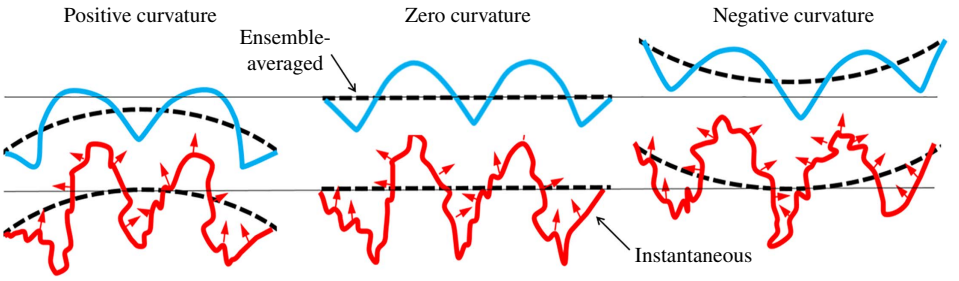

FIGURE 16. (Colour online) Schematic of the interaction of narrowband flame curvature with broadband turbulent wrinkling, following Shin & Lieuwen (2013).

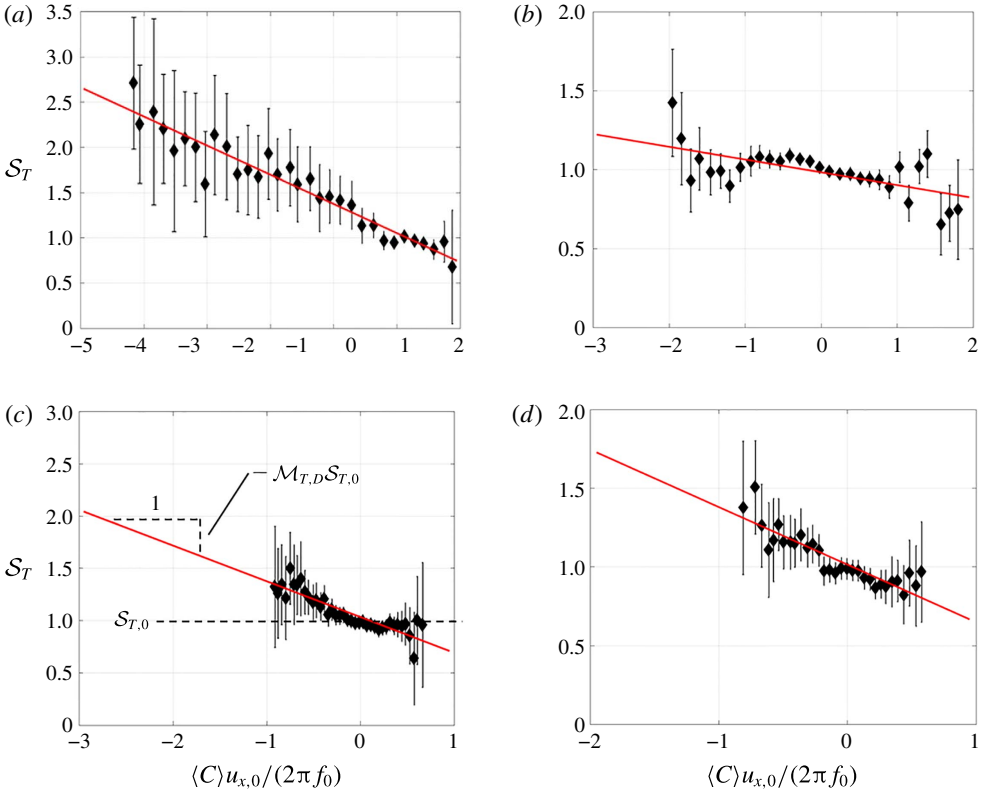

FIGURE 17. (Colour online) Dependence of the ensemble-averaged turbulent displacement speed upon ensemble-averaged curvature at four representative conditions, (*a*) $f_0 = 750$ Hz, $u_{x,0} = 4.8$ m s^{-1}, $u'/u_{x,0} = 9.3\,\%$, $\bar{C} = 0.5$, (*b*) $f_0 = 750$ Hz, $u_{x,0} = 7.0$ m s^{-1}, $u'/u_{x,0} = 27.3\,\%$, $\bar{C} = 0.5$, (*c*) $f_0 = 1250$ Hz, $u_{x,0} = 4.7$ m s^{-1}, $u'/u_{x,0} = 14.5\,\%$, $\bar{C} = 0.5$ (*d*) $f_0 = 1250$ Hz, $u_{x,0} = 6.2$ m s^{-1}, $u'/u_{x,0} = 32.1\,\%$.

curvature sensitivity as $\sigma_{T,D}$, because $\sigma_{T,D}$ cannot be recovered from values of $\mathcal{M}_{T,D}$, and *vice versa*, $\mathcal{M}_{T,D}$ is not directly proportional to the definition given in (1.5). These normalized values are also non-dimensional. In order to keep the figure readable, the curvature uncertainties are not shown in the following plots but the uncertainty in

normalized curvature is approximately 1.5–2.5 times the magnitude of the indicated S_T uncertainty for each data point.

Note the consistent flattening of S_T between approximately zero and unity curvature. This behaviour is evident in figure 17(*a*), but also occurs at other conditions and appears to approximately coincide with the region of higher data realizations (see figure 14). There are two possible explanations: (i) this flattening trend may be a bias error associated with non-uniform sampling of the curvature space. In other words, uncertainty in the curvature causes errors in estimation of the curvature in the high probability data region, (ii) this flattening may reflect a real change in the sensitivity of the flame speed to curvature for positive curvature values.

If the flattening reflects a real change in the flame speed, this indicates that for positive curvatures the relationship between curvature and flame speed changes. There are several features of premixed flames which can impact the flame response, including thermo-diffusive effects and the D–L instability. It is unlikely that the thermo-diffusive effect could account for this flattening. That is, for the thermo-diffusively stable reactant mixture examined in this work, this effect should further decrease the flame speed in the positive curvature regions rather than increase (and therefore flatten) the trend. A second possibility is that this flattening reflects the effect of the D–L instability. This explanation appears more likely as the hydrodynamic instability should cause wrinkle growth and thus would amplify wrinkles with positive curvature. Moreover, the most pronounced flattening at positive curvatures generally occurs for low and moderate turbulence intensity, where the hydrodynamic effect is expected to be most significant. This effect is discussed further below, in regard to figure 21. While this non-monotonic behaviour demonstrates that the flame response is not linear, utilizing a linear regression is, nonetheless, a convenient way to parameterize these results.

An interesting result of negative $S_{T,D}$ values is observed at the lowest turbulence intensities in some cases. Figure 18 shows a PDF illustrating the occurrence of some realizations of negative ensemble-averaged turbulent displacement speeds. In these cases, (particularly the 200 Hz, $U_{x,0} = 8$ m s^{-1} cases) negative $S_{T,D}$ values were observed at points near flame cusps. In most cases the negative flame speeds constitute only a small fraction of the overall realizations (such as shown in figure 14), and these instances fall within the absolute uncertainty of the measurements and calculations. However, the fact that this phenomenon is observed repeatedly (i) at the lowest turbulence intensity, and (ii) at locations of strong cusping suggests it is not simply an error. Moreover, it is well known that laminar and turbulent displacement speeds can become negative. This occurs when the reference isocontour moves in the same direction as the flow; in contrast, consumption-based flame speed definitions are always positive. For example, in locally laminar flames, negative displacement speeds occur for strongly stretched and curved flames (Sohrab, Ye & Law 1985; Gran *et al.* 1996; Chen & Im 1998; Lieuwen 2012; Trunk *et al.* 2013). It is important to point out that the displacement speeds measured in these studies of local flamelet dynamics are a fundamentally different quantity than the ensemble-averaged displacement speeds calculated in the current work, where the presence of negative ensemble-averaged turbulent flame speeds is a function of the definition and does not imply that instantaneous flame speeds are negative.

Furthermore, while there may appear to be analogies between the results presented in this study and the curvature sensitivity of the instantaneous displacement speed discussed in § 1, the underlying physical reasons are completely different. The instantaneous displacement speed exhibits curvature sensitivity because of Lewis

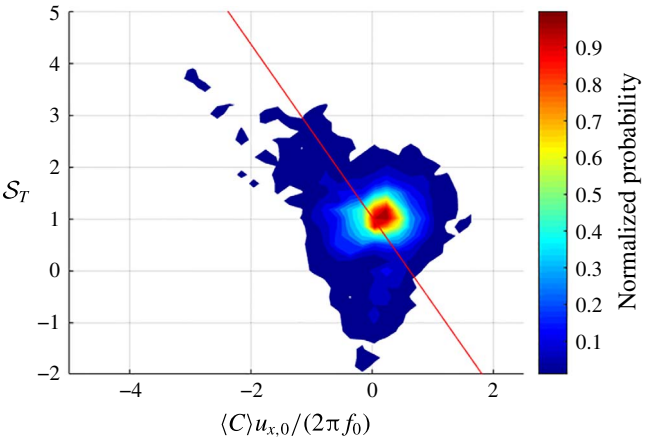

FIGURE 18. (Colour online) PDF plot of ensemble-averaged displacement speed versus ensemble-averaged curvature for a case showing realizations of negative flame speeds $f_0 =$ 750 Hz, $u_{x,0} = 7.9$ m s^{-1}, $u'/u_{x,0} = 9.8\,\%$.

number and differential mass diffusion rates. In contrast, the ensemble-averaged turbulent flame speed is fundamentally due to kinematic restoration effects associated with the fine-scale turbulence, as shown in figure 16; note that this effect occurs even if the instantaneous displacement speed exhibited no curvature sensitivity.

Returning to figure 17, these results can also be used to quantify the sensitivity of the flame speed modulation to curvature. Figure 19 shows the results for the 750 Hz case, while figure 21 shows the results for all cases. The value of $\mathcal{M}_{T,D}$ is estimated separately from both sides of the flame. Because this estimate of $\mathcal{M}_{T,D}$ is highly prone to noise induced from estimation of derivatives, we exclude cases (which differ between the left and right sides of the flame) where there are significant convecting velocity disturbance amplitudes (i.e. see discussion in context of figure 10) – this convecting disturbance introduces short length scale flame wrinkles which significantly amplify noise in estimates of flame position derivatives. This is done by only including cases where the maximum normal velocity perturbation magnitude, averaged over all phases, $\max(\bar{u}_{n,1}) < 0.55 S_{L,0}$.

Figure 19(a) plots results for the 750 Hz, 5 m s^{-1} case. It shows that the non-dimensional turbulent Markstein length is largely insensitive to the turbulence intensity. This is somewhat surprising as earlier isothermal work (Shin & Lieuwen 2013) indicated increasing sensitivity of the ensemble-averaged turbulent displacement speed with turbulence intensity; i.e. that $\mathcal{M}_{T,D}$ increases with u'. Thus, while figure 19(a) and above results confirm the sensitivity of the ensemble-averaged turbulent displacement speed to ensemble-averaged flame curvature, it indicates that this sensitivity does not increase with increasing turbulence. A potential resolution between these results is that the turbulence intensity examined in this work is significantly higher than that examined by (Shin & Lieuwen 2013). In fact, the highest turbulence intensity examined by Shin & Lieuwen (2013) is approximately equal to the lowest turbulence intensity examined in the current work (e.g. $u'/u_{x,0} \approx 0.10$, $u'/S_{L,0} \approx 0.40$). Thus, one possibility is that the increase in sensitivity observed previously occurs at relatively low turbulence intensity but saturates at higher turbulence levels. Indeed, there is good physical reason to expect such saturation; i.e. if the sensitivity of the ensemble-averaged flame speed

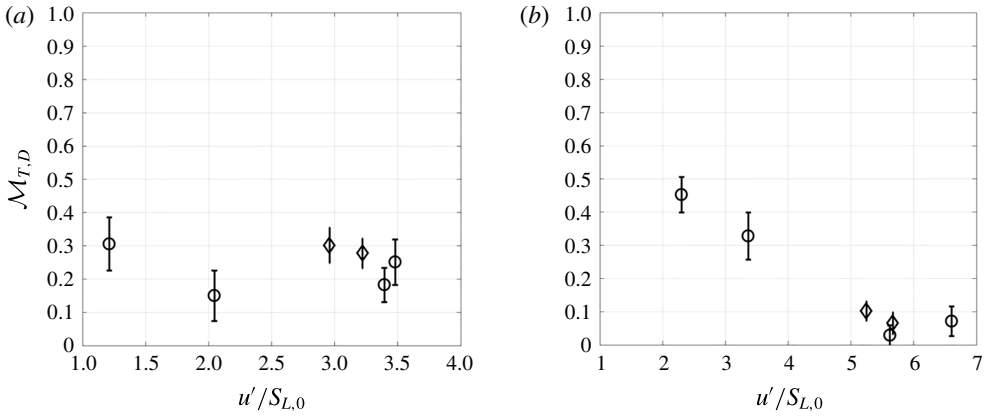

FIGURE 19. Calculated non-dimensional turbulent Markstein lengths at $f_0 = 750$ Hz, (*a*) for a nominal mean flow velocity $U_{x,0} = 5$ m s^{-1}, (*b*) for a nominal mean flow velocity $U_{x,0} = 8$ m s^{-1}. Circles indicate values determined from left side of the flame while diamonds indicate the right side of the flame.

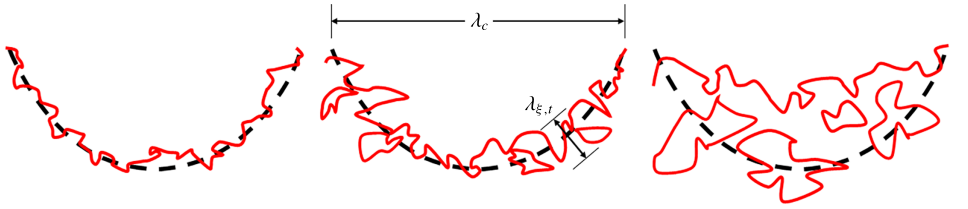

FIGURE 20. (Colour online) Schematic illustration of curvature sensitivity saturation with increasing turbulence intensity. The centre figure illustrates the convective, λ_c and turbulent flame, $\lambda_{\xi,t}$, length scales.

to curvature occurs due to mutual interaction and annihilation of opposing flame faces in negatively curved regions, as proposed by Shin & Lieuwen (2013) and discussed above in relation to figure 16, it seems likely that this mechanism would saturate at stronger turbulence, because once the flame faces interact, the mechanism of interaction is eliminated. This point is illustrated pictorially in figure 20; at low turbulence intensities where the magnitude of turbulence-induced flame wrinkling is small relative to the coherent flame wrinkle wavelength, these small-scale wrinkles increase the rate of coherent wrinkle destruction. In contrast, once the magnitude of these turbulence-induced wrinkles approaches the coherent wrinkling wavelength, the effect will saturate with increasing turbulent wrinkling amplitude.

Some support for this interpretation can be obtained from figure 19(*b*), obtained at a 60 % higher mean flow velocity, and therefore a longer convective wavelength ($\lambda_c = u_{x,0}/f_0$) than the lower mean flow results. Following the above argument, increasing the convective wavelength would delay saturation to higher turbulence intensities. Indeed, as figure 19(*b*) shows, $\mathcal{M}_{T,D}$ appears more sensitive to turbulence intensity at lower values of $u'/S_{L,0}$. Specifically, $\mathcal{M}_{T,D}$ is decreasing with turbulence intensity before reaching a nearly constant value of $\mathcal{M}_{T,D} \approx 0.075$ at the higher $u'/S_{L,0}$ values.

Figure 21 summarizes results from all cases where accurate $\mathcal{M}_{T,D}$ estimates can be obtained. As suggested by the discussion above, $\mathcal{M}_{T,D}$ is plotted as a function of the

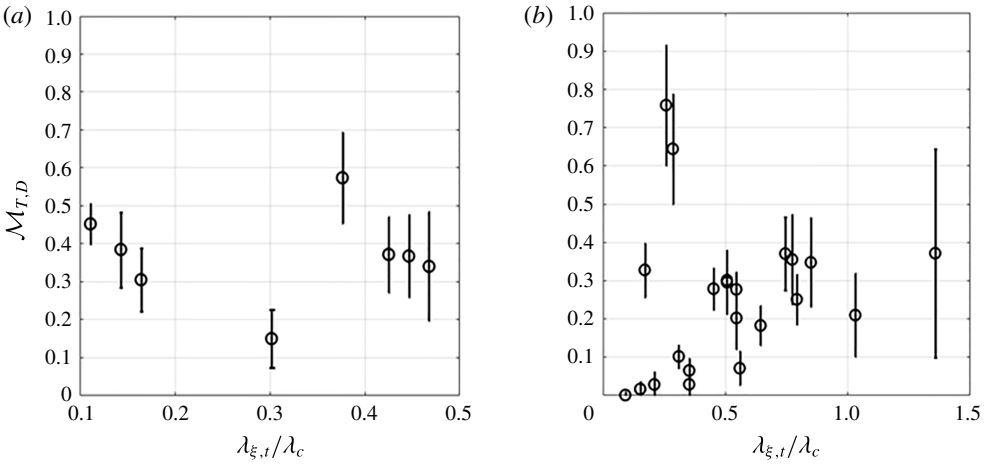

FIGURE 21. Normalized turbulent Markstein values for (*a*) data points with $u'/S_{L,0} \leqslant 2.5$, and (*b*) $u'/S_{L,0} > 2.5$ as a function of the ratio of turbulent flame wrinkling length to the coherent wrinkle length.

ratio of turbulent flame wrinkling amplitude, $\lambda_{\xi,t}$, normalized by the coherent flame wrinkle wavelength, $\lambda_c = u_{x,0}/f_0$. The turbulent flame wrinkling amplitude is scaled as $\lambda_{\xi,t} \propto u'\tau_{int}$, and τ_{int} denotes the integral turbulence time scale, estimated as $R/u_{x,0}$, where R is the jet radius.

The results in figure 21 suggest that the $\mathcal{M}_{T,D} = f(\lambda_{\xi,t}/\lambda_c)$ scaling captures some, but not all, of the sensitivity to turbulence intensity. Specifically, it suggests that $\mathcal{M}_{T,D}$ is independent of turbulence intensity for $\lambda_{\xi,t}/\lambda_c \sim O(1)$ (specifically $\lambda_{\xi,t}/\lambda_c >\sim 0.75$), with a value around 0.3. As discussed above, this may indicate that the global response saturates at higher $\lambda_{\xi,t}/\lambda_c$ values. Figure 21(*a*) shows data with $u'/S_{L,0} \leqslant 2.5$, while figure 21(*b*) shows data for $u'/S_{L,0} > 2.5$. Although the grouping is not completely homogeneous, it is evident that points in the higher $u'/S_{L,0}$ regime follow a different trend than for those with the lower $u'/S_{L,0} \leqslant 2.5$ values.

For the low $u'/S_{L,0}$ cases, figure 21(*a*), the normalized turbulent Markstein length appears generally insensitive to the ratio of turbulent and coherent length scales. On the other hand, for values of $u'/S_{L,0} > 2.5$, as shown in figure 21(*b*), there is nearly monotonic increase in the value of $\mathcal{M}_{T,D}$ with increasing wrinkling length scale ratio (the outlier points are discussed later). The different frequencies and flow velocities are distributed between both groupings; e.g. it is not that the 5 m s^{-1} velocity data fall into one set and the 8 m s^{-1} fall into the other (although because the grouping is based on $u'/S_{L,0}$, the higher values generally come from the 8 m s^{-1} cases).

The presence of the D–L instability may be the reason for these two groupings. We used the value of $u'/S_{L,0} = 2.5$ as a cutoff between these two regimes, based upon prior studies which suggests that the effect of the D–L instability upon turbulent flame dynamics diminishes as turbulence intensity increase. For example, Creta *et al.* (2016) numerically and experimentally examined the effect of the D–L instability on turbulent flames and found that for $u'/S_{L,0} > 2.5$ the otherwise abrupt changes associated with the onset of the instability were strongly diminished. In addition to the D–L instability, other factors also likely affect the results in the $u'/S_{L,0} \leqslant 2.5$ regime. For example, even after filtering the results to remove cases with unusably

large convecting disturbances, the low turbulence cases generally still contained the largest remaining induced velocity disturbances.

There are also several outlying values which occur for lower values of the length scale ratio in the $u'/S_{L,0} > 2.5$ regime. The two largest values in figure 21(*b*), at $\mathcal{M}_{T,D} \approx 0.65$ and $\mathcal{M}_{T,D} \approx 0.75$, are the result from a specific case ($f_0 = 1250$ Hz, $U_{x,0} = 8.0$ m s^{-1}, $u'/u_{x,0} \approx 14.0\,\%$), and it is possible that there is an unknown confounding variable in this case. Furthermore, consider that while the grouping used in figure 21 appears to separate the two groups quite well, the exact point of division is not obvious and these values may potentially fall into the other category, due to the various complicating effects discussed above. If these two outlying data points are neglected, the linear increase in $\mathcal{M}_{T,D}$ with increasing wrinkling length scale ratio, up to $\lambda_{\xi,t}/\lambda_c \approx 0.8$ is unmistakable, as shown in shown in figure 21(*b*).

The preceding discussion shows that in the low turbulence regime (i.e. $u'/S_{L,0} <$ 2.5–3.0) the ensemble-averaged results are potentially affected by the presence of the D–L instability and a high probability of convecting disturbances. Thus, in the low $u'/S_{L,0}$ regime the effect of turbulence on the ensemble-averaged turbulent displacement speed and its dependence on curvature is unclear. On the other hand, for $u'/S_{L,0} \gtrsim 2.5$ a distinct linear trend emerges, with the value of $\mathcal{M}_{T,D}$ increasing with the ratio of the wrinkling length scales, $\lambda_{\xi,t}/\lambda_c$ before saturating for values above $\lambda_{\xi,t}/\lambda_c \approx O(1)$. This result suggests that this $\lambda_{\xi,t}/\lambda_c$ parameter captures the sensitivity of $\mathcal{M}_{T,D}$ to turbulence intensity at higher $u'/S_{L,0}$ values.

4. Summary

This paper presented experimental results showing the interaction of turbulent flow disturbances with harmonic flame wrinkles. Harmonic perturbations are introduced on the flame through the use of an oscillating flame holder. Turbulence is introduced in the flow with the use of a variable turbulence generation system. Simultaneous Mie scattering and high speed PIV provide instantaneous flame edges and the instantaneous flow fields. The flame edges and flow fields are ensemble-averaged in order to determine the ensemble-averaged flame wrinkle dynamics and flow field.

The key contribution of this paper is showing that interactions between turbulent flow disturbances with harmonic flame wrinkling materially alter the ensemble-averaged flame dynamics. Specifically, the flame shape results show that increasing turbulence causes a decrease in amplitude of the harmonic flame wrinkles. These flame shape results are similar to those found in some previous isothermal computational studies.

Using the ensemble-averaged flame shape data and flow field, the ensemble-averaged, turbulent burning speed is calculated using a definition proposed by Shin & Lieuwen (2013). The ensemble-averaged turbulent burning speed, when averaged over all points of phase, increases in an approximately linear fashion with the flame coordinate. Furthermore, the phase-dependent turbulent burning speed shows dependence on the shape of the ensemble-averaged flame. Specifically, the flame speed increases where the ensemble-averaged flame curvature is negative. At low turbulence, and high mean flow velocity conditions, the strong wrinkling of the ensemble-averaged flame speed produces negative ensemble-averaged flame speeds, using the definition given in (1.4).

The sensitivity of the ensemble-averaged turbulent burning speed is quantified by calculation of the turbulent Markstein number. The results provide confirmation of the curvature sensitivity of ensemble-averaged flame speeds. It is suggested that the

turbulent Markstein number is controlled by the ratio of the turbulent flame wrinkling amplitude, and the coherent flame wrinkling wavelength for values of $u'/S_{L,0} \tilde{>} 2.5$–3.

Several additional studies are recommended as follow ons. First, while it is well-known quasi-coherent velocity disturbances are present in shear driven, high turbulence flows, these data clearly show the nonlinear interaction between the multi-scale turbulent disturbances and the more narrowband disturbances associated with coherent structures. In other words, conceptual models of controlling physics in combustors with shear driven turbulence must account for the fundamentally different effects of spectrally distributed turbulent disturbances and more narrowband, quasi-coherent disturbances. Future work should consider the effects of additional superposed velocity disturbances, such as two superposed coherent frequencies that are and are not integer multiples.

In addition, guiding theories are clearly needed for interpreting the results. Due to the inherent noisiness of the results, a result of taking second derivatives of data, several trends are confirmed but interpretation would benefit from a guiding theory. In addition, some of this noise can naturally be averaged out by increasing the size of data sets. This will be facilitated in the future as memory sizes in cameras continue to increase. Finally, additional study should be made of the modulation of the turbulent consumption speed. While consumption and displacement speeds generally exhibit qualitative similarities, they also can exhibit very different behaviours – a case in point is the negative displacement speeds observed in these measurements near cusps, a result that would not occur for consumption-based speeds.

Acknowledgements

The authors wish to thank T. Smith for his assistance with the laser diagnostic equipment and PIV processing. This research was partially supported by the Air Force Office of Scientific Research (contract no. FA9550-16-1-0442), contract monitor Dr. C. Li.

Supplementary movies

Supplementary movies are available at https://doi.org/10.1017/jfm.2017.728.

REFERENCES

BALACHANDRAN, R., AYOOLA, B. O., KAMINSKI, C. F., DOWLING, A. P. & MASTORAKOS, E. 2005 Experimental investigation of the nonlinear response of turbulent premixed flames to imposed inlet velocity oscillations. *Combust. Flame* **143**, 37–55.

BAUM, M., POINSOT, T. J., HAWORTH, D. C. & DARABIHA, N. 1994 Direct numerical simulation of H2/O2/N2 flames with complex chemistry in two-dimensional turbulent flows. *J. Fluid Mech.* **281**, 1–32.

BOYER, L. & QUINARD, J. 1990 On the dynamics of anchored flames. *Combust. Flame* **82**, 51–65.

CANDEL, S. & POINSOT, T. 1990 Flame stretch and the balance equation for the flame area. *Combust. Sci. Technol.* **70**, 1–15.

CHEN, J. H. & IM, H. G. 1998 Correlation of flame speed with stretch in turbulent premixed methane/air flames. *Symp. Intl Combust.* **27**, 819–826.

CRETA, F., LAMIONI, R., LAPENNA, P. E. & TROIANI, G. 2016 Interplay of Darrieus–Landau instability and weak turbulence in premixed flame propagation. *Phys. Rev.* E **94**, 053102.

DOWLING, A. P. 1999 A kinematic model of a ducted flame. *J. Fluid Mech.* **394**, 51–72.

DRISCOLL, J. F. 2008 Turbulent premixed combustion: flamelet structure and its effect on turbulent burning velocities. *Prog. Energy Combust. Sci.* **34**, 91–134.

DUCRUIX, S., DUROX, D. & CANDEL, S. 2000 Theoretical and experimental determination of the transfer function of a laminar premixed flame. *Proc. Combust. Inst.* **28**, 765–773.

EMERSON, B., MONDRAGON, U., ACHARYA, V., SHIN, D.-H., BROWN, C., MCDONELL, V. & LIEUWEN, T. 2013 Velocity and flame wrinkling characteristics of a transversely forced, bluff-body stabilized flame, part I: experiments and data analysis. *Combust. Sci. Technol.* **185**, 1056–1076.

FLEIFIL, M., ANNASWAMY, A. M., GHONEIM, Z. A. & GHONEIM, A. F. 1996 Response of a laminar premixed flame to flow oscillations: a kinematic model and thermoacoustic instability results. *Combust. Flame* **106**, 487–510.

GRAN, I. R., ECHEKKI, T. & CHEN, J. H. 1996 Negative flame speed in an unsteady 2-D premixed flame: A computational study. *Symp. Intl Combust.* **26**, 323–329.

HAWKES, E. R. & CHEN, J. H. 2004 Direct numerical simulation of hydrogen-enriched lean premixed methane–air flames. *Combust. Flame* **138**, 242–258.

HAWKES, E. R. & CHEN, J. H. 2006 Comparison of direct numerical simulation of lean premixed methane–air flames with strained laminar flame calculations. *Combust. Flame* **144**, 112–125.

HEMCHANDRA, S., PETERS, N. & LIEUWEN, T. 2011 Heat release response of acoustically forced turbulent premixed flames – role of kinematic restoration. *Proc. Combust. Inst.* **33**, 1609–1617.

HEMCHANDRA, S., PREETHAM & LIEUWEN, T. C. 2007 Response of turbulent premixed flames to harmonic acoustic forcing. *Proc. Combust. Inst.* **31**, 1427–1434.

HUMPHREY, L., ACHARYA, V., SHIN, D. H. & LIEUWEN, T. 2014 Technical note: Coordinate systems and integration limits for global flame transfer function calculations. *Intl J. Spray Combust. Dyn.* **6**, 411–416.

HUMPHREY, L. J., ACHARYA, V. S., SHIN, D.-H. & LIEUWEN, T. C. 2017 Modeling the response of turbulent flames to harmonic forcing. *Combust. Sci. Technol.* **189**, 187–212.

JIANG, G.-S. & PENG, D. 2000 Weighted ENO schemes for Hamilton–Jacobi equations. *SIAM J. Sci. Comput.* **21**, 2126–2143.

JONES, B., LEE, J. G., QUAY, B. D. & SANTAVICCA, D. A. 2011 Flame response mechanisms due to velocity perturbations in a lean premixed gas turbine combustor. *Trans ASME J. Engng Gas Turbines Power* **133**, 021503.

KABIRAJ, L. & SUJITH, R. I. 2012 Nonlinear self-excited thermoacoustic oscillations: intermittency and flame blowout. *J. Fluid Mech.* **713**, 376–397.

KASHINATH, K., HEMCHANDRA, S. & JUNIPER, M. P. 2013 Nonlinear thermoacoustics of ducted premixed flames: The influence of perturbation convection speed. *Combust. Flame* **160**, 2856–2865.

KEE, R. J. *et al.* 2011 *CHEMKIN 10112*. Reaction Design.

KERL, J., LAWN, C. & BEYRAU, F. 2013 Three-dimensional flame displacement speed and flame front curvature measurements using quad-plane PIV. *Combust. Flame* **160**, 2757–2769.

KERSTEIN, A. R., ASHURST, W. T. & WILLIAMS, F. A. 1988 Field equation for interface propagation in an unsteady homogeneous flow field. *Phys. Rev.* A **37**, 2728–2731.

KORNILOV, V. N., SCHREEL, K. R. A. M. & DE GOEY, L. P. H. 2007 Experimental assessment of the acoustic response of laminar premixed Bunsen flames. *Proc. Combust. Inst.* **31**, 1239–1246.

LAVISION 2016 *FlowMaster PIV/PTV-systems*. http://www.lavision.de/en/products/flowmaster/index.php.

LAW, C. K. & SUNG, C. J. 2000 Structure, aerodynamics, and geometry of premixed flamelets. *Prog. Energy Combust. Sci.* **26**, 459–505.

LIEUWEN, T. C. 2012 *Unsteady Combustor Physics*. Cambridge University Press.

LIEUWEN, T. C. & YANG, V. (Eds) 2005 *Combustion Instabilities in Gas Turbine Engines: Operational Experience, Fundamental Mechanisms, and Modeling*. American Institute of Aeronautics and Astronautics.

LING, L., TIANYI, Z., LAWRENCE, K. & WEI, Z. 2007 Ordinary least square regression, orthogonal regression, geometric mean regression and their applications in aerosol science. *J. Phys: Conf. Ser.* **78**, 012084.

LIPATNIKOV, A. 2012 *Fundamentals of Premixed Turbulent Combustion*. CRC Press.

LIPATNIKOV, A. & CHOMIAK, J. 2007 Global stretch effects in premixed turbulent combustion. *Proc. Combust. Inst.* **31**, 1361–1368.

LIPATNIKOV, A. N. & SATHIAH, P. 2005 Effects of turbulent flame development on thermoacoustic oscillations. *Combust. Flame* **142**, 130–139.

MAGRI, L. & JUNIPER, M. P. 2013 A Theoretical approach for passive control of thermoacoustic oscillations: application to ducted flames. *Trans ASME J. Engng Gas Turbines Power* **135**, 091604.

MARSHALL, A., VENKATESWARAN, P., NOBLE, D., SEITZMAN, J. & LIEUWEN, T. 2011 Development and characterization of a variable turbulence generation system. *Exp. Fluids* **51**, 611–620.

MATALON, M. 2009 Flame dynamics. *Proc. Combust. Inst.* **32**, 57–82.

MATALON, M. & CRETA, F. 2012 The 'turbulent flame speed' of wrinkled premixed flames. *C. R. Méc.* **340**, 845–858.

MATALON, M. & MATKOWSKY, B. J. 1982 Flames as gasdynamic discontinuities. *J. Fluid Mech.* **124**, 239–259.

OTSU, N. 1979 A threshold selection method from gray-level histograms. *IEEE Trans. Syst. Man Cybern.* **9**, 62–66.

PETERS, N., WENZEL, H. & WILLIAMS, F. A. 2000 Modification of the turbulent burning velocity by gas expansion. *Proc. Combust. Inst.* **28**, 235–243.

PETERSEN, R. E. & EMMONS, H. W. 1961 Stability of laminar flames. *Phys. Fluids* **4**, 456–464.

POINSOT, T. & VEYNANTE, D. 2005 *Theoretical and Numerical Combustion*. RT Edwards, Inc.

PREETHAM, S. H. & LIEUWEN, T. 2008 Dynamics of laminar premixed flames forced by harmonic velocity disturbances. *J. Propul. Power* **24**, 1390–1402.

SANKARAN, R., HAWKES, E. R., CHEN, J. H., LU, T. & LAW, C. K. 2007 Structure of a spatially developing turbulent lean methane-air Bunsen flame. *Proc. Combust. Inst.* **31**, 1291–1298.

SANTOSH, H. & SUJITH, R. 2005 Kinematic coupling effects on heat-release transfer function of a premixed flame. *J. Propul. Power* **21**, 591–599.

SEARBY, G., TRUFFAUT, J.-M. & JOULIN, G. 2001 Comparison of experiments and a nonlinear model equation for spatially developing flame instability. *Phys. Fluids* **13**, 3270–3276.

SHANBHOGUE, S., SHIN, D.-H., HEMCHANDRA, S., PLAKS, D. & LIEUWEN, T. 2009 Flame-sheet dynamics of bluff-body stabilized flames during longitudinal acoustic forcing. *Proc. Combust. Inst.* **32**, 1787–1794.

SHIN, D.-H. & LIEUWEN, T. 2012 Flame wrinkle destruction processes in harmonically forced, laminar premixed flames. *Combust. Flame* **159**, 3312–3322.

SHIN, D. H. & LIEUWEN, T. C. 2013 Flame wrinkle destruction processes in harmonically forced, turbulent premixed flames. *J. Fluid Mech.* **721**, 484–513.

SHIN, D.-H., PLAKS, D. V., LIEUWEN, T., MONDRAGON, U. M., BROWN, C. T. & MCDONELL, V. G. 2011 Dynamics of a longitudinally forced, bluff body stabilized flame. *J. Propul. Power* **27**, 105–116.

SMITH, G. P. *et al.* 1999 *GRI-Mech 3.0* chemical mechanism. Available at: http://www.me.berkeley.edu/gri_mech/.

SOHRAB, S. H., YE, Z. Y. & LAW, C. K. 1985 An experimental investigation on flame interaction and the existence of negative flame speeds. *Symp. Intl Combust.* **20**, 1957–1965.

TAMMISOLA, O. & JUNIPER, M. P. 2016 Coherent structures in a swirl injector at $Re = 4800$ by nonlinear simulations and linear global modes. *J. Fluid Mech.* **792**, 620–657.

TRUFFAUT, J.-M. & SEARBY, G. 1999 Experimental Study of the Darrieus–Landau instability on an inverted-'V' flame, and measurement of the Markstein number. *Combust. Sci. Technol.* **149**, 35–52.

TRUNK, P. J., BOXX, I., HEEGER, C., MEIER, W., BÖHM, B. & DREIZLER, A. 2013 Premixed flame propagation in turbulent flow by means of stereoscopic PIV and dual-plane OH-PLIF at sustained kHz repetition rates. *Proc. Combust. Inst.* **34**, 3565–3572.

WANG, H. Y., LAW, C. K. & LIEUWEN, T. 2009 Linear response of stretch-affected premixed flames to flow oscillations. *Combust. Flame* **156**, 889–895.

WHEELER, A. J. & GANJI, A. R. 1996 *Introduction to Engineering Experimentation*. Prentice Hall.

WILLIAMS, F. A. 1985 Turbulent combustion. In *The Mathematics of Combustion* (ed. J. D. Buckmaster), pp. 267–294. Society for Industrial and Applied Mathematics.